applied sciences

MDPI

Article

Performance of Steel-Bolt-Connected Industrialized Building System Frame Subjected to Hydrodynamic Force

Abubakar Sharif Auwalu [1,*], Norhazilan Md Noor [2], Mohamad Shazwan Ahmad Shah [1], Sarehati Umar [1], Mugahed Amran [3,4,*], Musa Adamu [5], Nikolai Ivanovich Vatin [6] and Roman Fediuk [6,7]

[1] School of Civil Engineering, Faculty of Engineering, Universiti Teknologi Malaysia, Skudai 81310, Johor, Malaysia; mohamadshazwan@utm.my (M.S.A.S.); sarehati@utm.my (S.U.)
[2] Construction Research Centre, School of Civil Engineering, Faculty of Engineering, Universiti Teknologi Malaysia, Skudai 81310, Johor, Malaysia; norhazilan@utm.my
[3] Department of Civil Engineering, College of Engineering, Prince Sattam Bin Abdulaziz University, Alkharj 16273, Saudi Arabia
[4] Department of Civil Engineering, Faculty of Engineering and IT, Amran University, Amran 9677, Yemen
[5] Engineering management Department, College of Engineering, Prince Sultan University, Riyadh 11586, Saudi Arabia; madamu.civ@buk.edu.ng
[6] Peter the Great St. Petersburg Polytechnic University, St. Petersburg 195251, Russia; vatin@mail.ru (N.I.V.); fedyuk.rs@dvfu.ru (R.F.)
[7] Polytechnic Institute, Far Eastern Federal University, Vladivostok 690922, Russia
* Correspondence: asausharif2@gmail.com (A.S.A.); m.amran@psau.edu.sa (M.A.)

Abstract: People need durable shelters for living safely due to devastation caused by flooding in some areas, and it is not easy to mitigate the frequency and intensity of the flooding. Therefore, in this research, an industrialized building system (IBS) has been proposed as one of the best solutions. However, most of the existing IBSs were not designed and tested for resisting a sudden horizontal impact. Furthermore, the joints of some IBSs would likely be vulnerable to failure when subjected to a horizontal impact. There is a need to develop a bolt-connected IBS that is able to withstand a horizontal impact load. Thus, this study aimed to investigate the performance of steel-bolt-connected IBS frames subjected to the sudden impact of hydrodynamic force. Autodesk computational fluid dynamic (CFD) simulation was used for optimizing the laboratory experiment. A 1:5-scale IBS frame was designed and tested for the dam-break test using 1 m, 2 m, and 3 m reservoir water levels. The results showed that the bolt connections were very effective and robust in the IBS frame. They also restricted damages from spreading to other structural components due to energy dissipation. The main findings of this study are crucial to improving the current IBS method of construction.

Keywords: industrial building; dam break; CFD simulation; steel bolt; reservoir water level

Citation: Auwalu, A.S.; Noor, N.M.; Shah, M.S.A.; Umar, S.; Amran, M.; Adamu, M.; Vatin, N.I.; Fediuk, R. Performance of Steel-Bolt-Connected Industrialized Building System Frame Subjected to Hydrodynamic Force. *Appl. Sci.* **2022**, *12*, 5093. https://doi.org/10.3390/app12105093

Academic Editor: Amadeo Benavent-Climent

Received: 15 April 2022
Accepted: 17 May 2022
Published: 18 May 2022

1. Introduction

Flooding is a well-known, ongoing, serious problem worldwide, especially in countries such as Russia, Malaysia, Nigeria, China, UK, Nepal, USA, Thailand, and Ecuador. Several major floods have been experienced within the last decade [1–8]. Flooding is typically categorized into two types: heavy rains (monsoon) floods and flash flooding [9]. Floods are a natural hazard that seriously threatens sustainable development, and they also cause environmental damage [10]. It is also well known that floods usually destroy people's houses and property, cause displacements and loss of life, pose health risks, and adversely affect people's livelihoods, thereby accentuating poverty. With the advent of climate change, floods have been projected to increase in frequency and intensity in many parts of the world [11,12]. About 350 million people worldwide are affected by floods, and it has been forecasted that flood devastation will double by the end of 2050

[13]. From 1996 to 2015, around 150,061 flood events occurred globally and were responsible for 11.1% of global disaster fatalities, based on the information from the United Nations Office for Disaster Risk Reduction (UNISDR) [14,15]. Researchers and scientists have found that the main causes of floods tend to be both natural and anthropogenic, including climate change, deforestation, increasing population, environmental degradation, and intensified land use. Thus, the effect of flooding restricts the sustainable development of economies and societies [7].

There is anticipation of frequent extreme flooding every year in some parts of the globe due to heavy monsoon rainfall [5–7,10,16]. The stationary assumption has been challenged in recent years due to increased extreme weather, potentially leading to underestimating flood quantiles and an increased risk of structural failures [6]. Chen concentrates on flood frequency mitigation, while many current studies concentrate on the recovery stage of the flood because flooding destroys infrastructures [5–7,10]. Therefore, come studies concentrate on the recovery framework, which involves building a permanent settlement by producing a building system in which the structures can be built quickly and must be robust and cheap [17,18]. There are many proposed solutions, which include: containers, modular blocks, and industrialized building system (IBS) frame structures that are readily available in the local market. IBSs have been acknowledged as one of the best solutions with some shortcomings. The performance of IBSs has not been fully investigated, especially the performance and the behavior at the joint [19]. Since floods with debris move at high speed, the sudden impact imposed by a flood with debris onto the sidewall of a permanent settlement may cause failure, especially at the joint.

IBSs have been proposed as one of the best solutions for building a permanent settlement in flood-prone zones experiencing extreme flood disasters. IBS can offer speedy site assembly with high-quality construction; this makes it the best candidate for rebuilding post-disaster permanent settlements [15,20]. Moreover, IBSs are very strong for sustaining vertical loads, but most of them were not designed to sustain horizontal sudden impact loads, especially at the joint [18,21–23]. Since some of the existing IBSs were not designed to sustain the horizontal impact of floods with debris, the construction of newly built permanent settlements could be destroyed by floods in the next cycle. Hence, the cost of flood disaster recovery will increase in the long term. However, studies on the behavior and performance of IBSs subjected to horizontal impact are lacking. Furthermore, the joint of an IBS is likely to be more vulnerable to failure when subjected to horizontal load. Chikun [24], Al-Sabah [25], and Bong [26] proposed an effective steel frame system and evaluated the structural performance of its beam–column connection through experimental and analytical work. Hence, the behavior of steel frame performance is different from concrete structures connected with steel bolts. Wei [27] investigated beam–column-assembled joint connections, focusing on the mechanical properties of a new dry-type high-strength bolt connection joint used in prefabricated buildings. However, Wei [27] stated that their study results provided a foundation for the analysis of assembled structural framework systems based on different forms of dry-type connection joints. Hence, this means that there is a need for investigating the performance of a steel-bolt-connected IBS frame structure for sudden horizontal impact in order to obtain more reliable results.

Despite the fact that Lacerda [28], Al-Salloum [29], Mokhtar [30], and Wong [31] investigated different types of IBS steel bolt connections, they have not solved all the connection problems in IBSs. Some of the types of connections covered in these studies could be catastrophic to future structures. When a shared failure occurs in some of those connections, the whole building can completely collapse. There is, therefore, a need to develop a building system where the failure of one component will not cause the collapse of the whole structure, so that future structures can avoid shear failure, as in the findings of Al-Salloum [29]. Hence, steel-bolt-connected IBSs would be able to withstand the horizontal impact of the flood.

Nevertheless, based on the current literature, as reported by Jabar [21] and Chidambaram [23], the performance and behavior of steel bolt connections are still in their infancy stage. Therefore, this study aims to investigate the bolt connection performance and its behavior subject to the sudden impact of horizontal hydrodynamic force against steel-bolt-connected IBS frames using computational fluid dynamics (CFD) simulation software and experimental work.

The steel-bolt-connected IBS frame was simulated in CFD software for optimizing the experimental laboratory test. A steel-bolt-connected IBS frame was fabricated and tested for the horizontal impact of hydrodynamic force against the structure to understand the clear effectiveness of the steel bolt connection technique. The steel bolt connection has proven to be very effective. It resisted high impacts of hydrodynamic forces without a sign of failure, leading to the additional robustness of the IBS. This high resistance can potentially become the best solution for flood-prone zone structures in the future. This study successfully explored the potential of the IBS bolt connection subject to a sudden horizontal impact as one of the best solutions to the connection problems of the IBS method.

2. Design Methods

Autodesk CFD was used for collecting the necessary data prior to the laboratory work. The existing experimental design and results for a full-scale model were used during the simulation for optimizing the experimental work. The laboratory work, using 1:5-scale models, was conducted to investigate the performance and the behavior of steel-bolt-connected IBS structures under the sudden horizontal impact of hydrodynamic force. The tested structure was a two-dimensional steel-bolt-connected IBS frame component. The computational fluid dynamic was performed using Autodesk Simulation CFD to gain an understanding of the behavior of steel-bolt-connected structures, which was later used to optimize the experimental work. Figure 1 presents the stage of laboratory work.

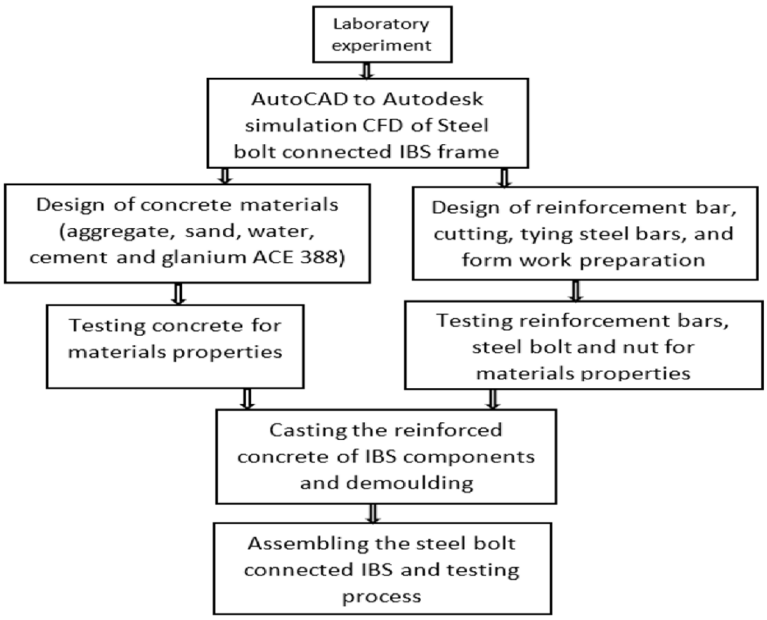

Figure 1. Summary of the experimental work.

2.1. Modelling and Similitude Law

The scaled-down model of 1:5 scale is well known and it has been used for experimental investigations of full-scale structures due to the time factor, limitations in the capacities of testing facilities, and the fact that experimentation on scaled models costs less

[31–39]. For the experiments to be successful, all structural models must be designed and loaded, and the results of the experimental data must be analyzed suitably [40]. These can be achieved through the following similitude requirements.

2.1.1. Geometric Similarity

The prototype and model must have the same shape, but they can have different sizes. The requirements for geometric similarities are satisfied if the shape of the reducing model (m) of any object corresponds exactly to the prototype *(p)*. It involves the reduction in all dimensions at the same scale. If M_x = L_{px}/L_{mz}, M_y=, L_{py}/L_{my}, and M_z = L_{pz}/L_{mz} are considered as the scaling numbers for this research, then the following equilibrium $Mx = My = Mz$ should be established in modelling details [40,41].

However, to achieve true dynamic similarity, all the dimensionless parameters (π terms) must possess the same value in both the model (m) and the prototype (*p*) (Equation (1) [40]).

$$Fr_p = Fr_m,\ Eu_p = Eu_m,\ Re_p = Re_m,\ We_p = We_m,\ Ma_p = Ma_m \quad (1)$$

The mechanical similarity can be established if both conditions for geometrically and dynamic similarities are satisfied for modeling. Hence, the mechanical similarity is assumed for all modeling stages in this research.

The basic variables that are commonly used in hydraulic research are the following: geometry (length, *L)*; flow properties (velocity, *V* m/s); pressure difference, ΔP (Pa); fluid properties (density of water, ρ (kg/m^3)); the dynamic viscosity of water, μ (N s/m^2); the surface tension of air and water, σ (N/m); the bulk modulus of elasticity of water, Eb (Pa); the acceleration of gravity, g (m/s^2). The following are the three basic dimensions that are commonly used in fluid mechanics: mass *(M)*, length *(L),* and time *(t)*.

Buckingham [42] stated that the pi theorem implies that the quantities can be grouped into five (5 = 8 − 3) independent, dimensionless parameters, expressed in Equations (2a) and (2b) [40].

$$F_2\left(\frac{V}{\sqrt{gL}};\ \frac{\rho V^2}{\Delta P};\ \frac{\rho VL}{\mu};\ \frac{V}{\sqrt{\frac{\sigma}{\rho L}}};\ \frac{V}{\sqrt{\frac{E_b}{\rho}}}\right) \quad (2a)$$

$$F_2\ \ (F_r;\ E_u;\ R_e;\ W_e;\ M_a) \quad (2b)$$

The ratios Fr, Eu, Re, We, and Ma are for Froude number *(F_r)*, Euler number *(E_u)*, Reynolds number *(R_e)*, Weber number *(W_e)*, and Sarrau–Mach number *(M_a)*, respectively.

2.1.2. Kinematic Similarity

Model and prototype flow fields are kinematically similar when the velocities at corresponding points are the same in each direction and differ only by a constant factor of velocity ratio, Vr. In other words, if the quantities are related to motions, the similarity is called kinematic similarity. However, this refers to the similarity of motion, and motions are described by distance and time, which implies similarity of lengths (i.e., geometrical similarity) and the similarity of time intervals [40,41].

$$\text{Velocity} = \frac{V_m}{V_p} = \frac{L_m/T_m}{L_P/T_p} = \frac{L_m}{L_p} \div \frac{T_m}{T_p} = \frac{L_r}{T_r}. \quad (3)$$

$$\text{Acceleration} = \frac{a_m}{a_p} = \frac{L_m/T_m^2}{L_P/T_p^2} = \frac{L_m}{L_p} \div \frac{T_m^2}{T_p^2} = \frac{L_r}{T_r^2} \quad (4)$$

$$\text{Discharge} = \frac{Q_m}{Q_p} = \frac{L_m^3/T_m}{L_p^3/T_p} = \frac{L_m^3}{L_p^3} \div \frac{T_m}{T_p} = \frac{L_r^3}{T_r} \quad (5)$$

2.2. Construction of 1:5-Scaled IBS Components

Testing a full-scale IBS frame was not chosen due to fabrication and testing issues. Therefore, a scale of 1:5 residential units was constructed in the laboratory to simplify the

laboratory works and reduce the cost of the experimental tests. The following section discusses the construction of downscaled specimens, scaled to 1:5 according to their full-scale configurations.

2.2.1. Materials Properties of the IBS Concrete

The OPC used complied with the Type I Portland cement, as in ASTM C150-05 [43] and BS12:1991 [44]. Water is one of the most important constituents, and without it, concrete cannot be produced. It should not contain any substance which can be harmful to the process of hydration of cement and the durability of concrete. Water which is acceptable for drinking is also suitable for concrete mixing [45]. Therefore, normal tap water was used to produce the concrete specimens for IBS components casting during the mixing process. Crushed stones obtained from the quarry with a size of less than 5 mm were used as coarse aggregates. According to DOE, the coarse aggregate was air-dried to obtain saturated surface dry conditions to ensure that the water–cement ratio was not affected. Gradation, moisture content, shapes, and texture are some of the characteristics of aggregate, which could affect the workability and bond in the concrete matrix. The gradation was in accordance with the specifications of ASTM C33-03 [46].

Fine aggregate is usually known as sand, which must comply with coarse, medium, or fine grading. The sand used was dried initially in the laboratory oven at the temperature of 105 ± 5 °C. After that, it was sieved accordingly. The sand used was as per the specifications of ASTM C778-02 [47]. The fineness modulus was found to be 2.36 mm. Glenium ACE 388 brand of polycarboxylic obtained from the chemical industry was used as a superplasticizer (SP) for workability, and it was available in the form of a dark-brown liquid. Hence, the amount of Glenium ACE 388 used in this research mixes was 1.2% of the cement volume. The mix design of this research was made to achieve the characteristic strength of 30 N/mm^2 at 28 days of curing for making IBS components. Thereafter, several mixed were made for obtaining the target strength. The materials used were crushed aggregate (4.75 mm), fine aggregate passing 2.36 mm, Ordinary Portland Cement, tap water, and Glenium (Superplasticizer) ACE 388. The concrete mix design proportion was 1: 2: 0.9: 0.42 (cement: aggregate: sand: water). The quantity of Glenium ACE 388 (superplasticizer) used was 1.2% of cement volume. Figure 2a–d presents the concrete materials, while Table 1 presents the proportion of concrete materials and the admixture design. It was made based on guidance from the British Research Establishment (BRE).

(**a**)

(**b**)

(**c**)

(**d**)

Figure 2. Illustrations of the concrete materials: (**a**) fine aggregate in the oven; (**b**) coarse aggregate; (**c**) Glenium ACE 388; (**d**) mixing process.

Table 1. The proportions of concrete materials.

Quantity	Cement (kg)	Water (kg)	Coarse Aggregate (kg)	Fine Aggregate (kg)	Glenium ACE 388 (kg)
Per (m^3)	550	233	1086	511	6.6

The downscaled model utilized steel bars with diameters of 6 mm for the main reinforcement and 2 mm as the tie reinforcements. Twelve concrete cylinder samples with the size of 50 mm × 100 mm were tested for compressive strength and tensile strength at 7 days and 28 days of curing. Three samples were tested for each material properties test at 7 days and 28 days of curing. The tested samples are shown in Figure 2a–d for compressive strength and splitting tensile strength. Their corresponding properties are tabulated in Tables 2 and 3 as well. The split tensile strength was accomplished according to ASTM C496-96 [48]. The compression and tensile tests were conducted to obtain the concrete's compressive and tensile strength, respectively. Compressive strength was obtained to predict the concrete crush, while tensile strength predicts concrete cracks during laboratory testing.

ASTM C39 [49] provides testing procedures to determine the compressive strength and tensile properties of concrete. However, for downscaled models, the selection of smaller-sized control cylinders can have a considerable variation in the compressive strength [50]. The ACI committee 444, Models of concrete structures, recommends the use of 2 × 4 in (50 mm × 100 mm) cylinders as the standard testing specimen to obtain a characteristic of concrete strength for model studies [51]. Figure 3a–d shows the tested samples for compression and splitting tensile.

(**a**)

(**b**)

(**c**) (**d**)

Figure 3. Testing of concrete cylinders: (**a**) cylinder under compressive test; (**b**) cylinders after compression tests; (**c**) cylinder under splitting test; (**d**) cylinders after splitting tests.

Tables 2 and 3 showed the compressive strength results of twelve cylinders with the size of 50 mm × 100 mm for 7 days and 28 days of curing. It has been tested by using a concrete compression testing machine. The obtained compressive strength at 28 days was 31.38 N/mm^2. Hence, the obtained average of compressive strength for the concrete cylinders met the target of grade C30 mixture with superplasticizer, indicating very promising results for obtaining the desired strength at 28 days.

Table 2. Compressive strength for 7 days of curing.

Number of Sample	Force (kN)	Strength (N/mm^2)	Displacement (mm)	Strain
1	44.18	22.50	2.11	0.0211
2	38.76	19.74	2.42	0.0242
3	44.46	22.64	2.51	0.0251
4	48.51	24.70	2.52	0.0252
5	42.42	21.60	2.32	0.0232
6	45.36	23.10	2.61	0.0261
Average	43.95	22.38	2.42	0.0242

Table 3. Compressive strength for 28 days of curing.

Number of Sample	Force (kN)	Strength (N/mm^2)	Displacement (mm)	Strain
1	59.11	30.10	3.01	0.03
2	58.25	29.66	2.87	0.03
3	62.51	31.83	3.13	0.03
4	65.20	33.20	3.57	0.04
5	61.47	31.30	3.09	0.03
6	63.23	32.20	3.32	0.03
Average	61.63	31.38	3.17	0.03

The compressive strength was obtained to predict the concrete crush, while the tensile strength is to forecast concrete cracks during laboratory testing on the system. The obtained average of splitting tensile strength of concrete cylinders for 7 days and 28 days of curing for structural model tests are 0.582 N/mm^2 and 1.223 N/mm^2, respectively. Tables 4 and 5 show their respective results.

Table 4. Splitting tensile test for 7 days of curing.

Number of Sample	Force (kN)	Strength (Mpa)
1	0.82	0.75
2	0.72	0.68
3	0.70	0.65
4	0.58	0.54
5	0.48	0.44
6	0.44	0.43
Average	0.62	0.58

Table 5. Splitting tensile test for 28 days of curing.

Number of Sample	Force (kN)	Strength (Mpa)
1	1.03	0.87
2	1.21	1.02
3	1.11	0.99
4	1.32	1.21
5	1.63	1.53
6	1.82	1.72
Average	1.35	1.22

2.2.2. Properties of the IBS Steel Bars and the Steel Bolts

All the specified steel bars and the steel bolts for this experimental work were firstly tested in the laboratory to obtain their actual mechanical properties. Figure 4a–c shows the tested specimens. The mechanical properties of the steel bars and steel bolts, such as ultimate stress, ultimate strain, and displacement, obtained from the test, are listed in Tables 6–8, respectively.

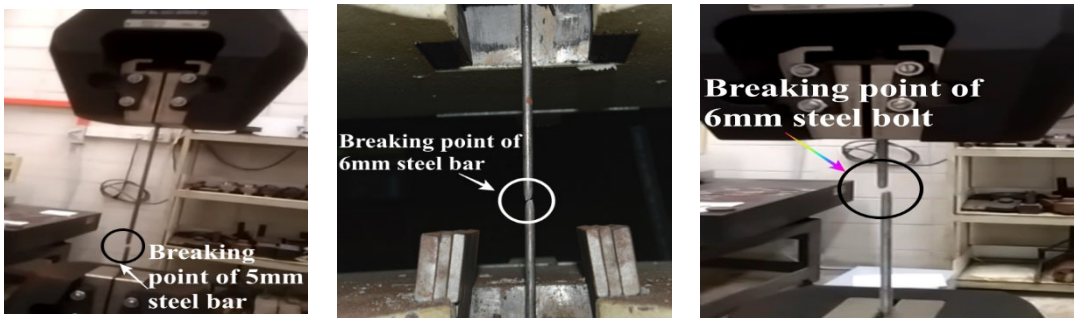

(**a**) (**b**) (**c**)

Figure 4. Splitting tensile test: (**a**) 5 mm steel bar; (**b**) 6 mm steel bar; (**c**) 6 mm steel bolt.

Table 6. Results for 5 mm-diameter steel bars.

No. of Sample	Force (kN)	Stress (Mpa)	Max Displacement (mm)	Strain
1	12.05	613.95	7.91	5.75
2	11.51	586.25	5.37	4.49
3	11.53	587.15	7.35	5.48
Average	11.70	595.78	6.87	5.24

Table 7. Results for 6 mm-diameter steel bars.

No. of Sample	Force (kN)	Stress (Mpa)	Max Displacement (mm)	Strain
1	15.19	37.33	1.86	1.86
2	16.16	571.55	0.73	1.34

3	17.02	601.97	5.59	3.94
Average	16.12	570.28	2.73	2.38

Table 8. Results for 6 mm-diameter steel bolts.

No. of Sample	Force (kN)	Stress (Mpa)	Max Displacement (mm)	Strain
1	10.91	385.95	4.50	3.65
2	11.06	391.30	3.71	3.95
3	10.98	388.41	3.15	6.09
Average	10.99	388.55	3.79	4.56

The downscaled model utilized steel bars with diameters of 6 mm and 2 mm as the main reinforcements and the shear links for columns, beams, slabs, and footing, respectively. Based on Figure 5a,b, the column head has 24 steel reinforcement bars for making the corbels support. The diameter of the bars is 6 mm, while the length is 200 mm. There are three main reinforcements in two faces of the column and one main reinforcement bar in other faces with a length of 680 mm. A total of 23 square links were used to tie up the main column reinforcement with the spacing of 30 mm between each square link. Four aluminum pipes with diameters of 8 mm were installed at each corner of the column and tied up with the edge reinforcement for a bolt slot to connect the structures.

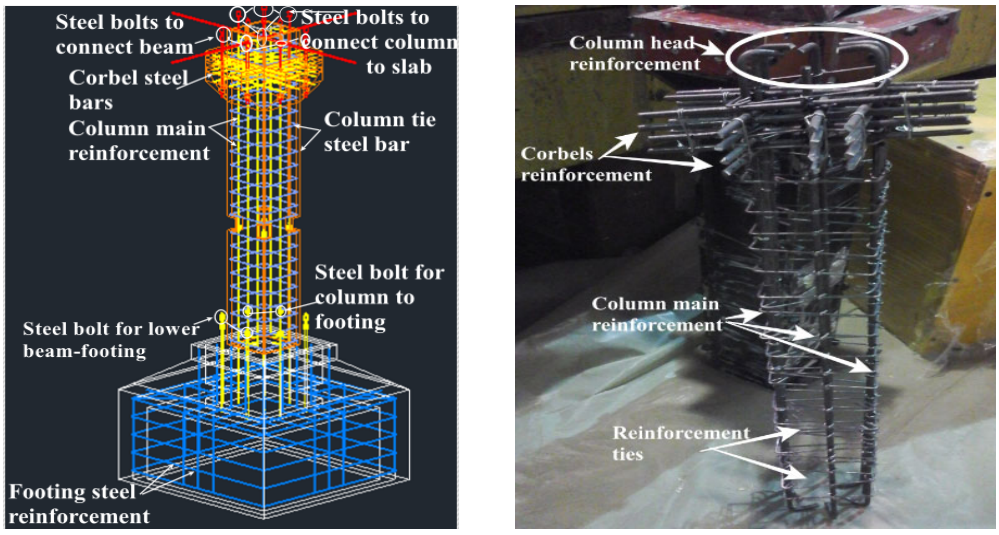

(**a**) (**b**)

Figure 5. Column reinforcement details: (**a**) AutoCAD details; (**b**) actual column details.

The scaled-down footing has three different 6 mm reinforcement bars configurations in it. There are five steel bars around the footing with 40 mm spacing to each other. Three reinforcement bars were installed vertically on four faces of the footing. At the top of the footing from the sloping parts, there is one horizontal steel bar at each face of the footing. Figure 6a,b show the reinforcements detailing for the footing.

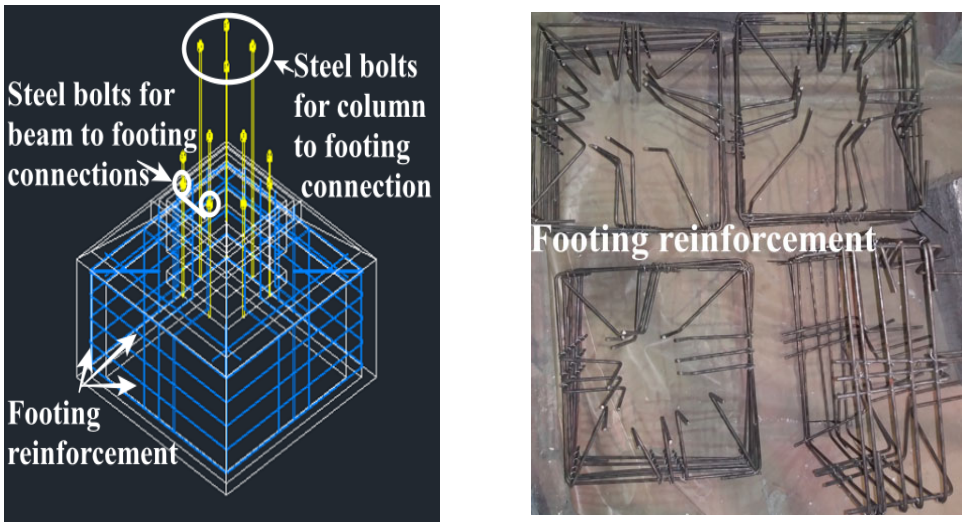

(**a**) (**b**)

Figure 6. Footing reinforcement details: (**a**) AutoCAD details; (**b**) actual footing details.

The structural beam has five steel reinforcement bars, two at the top in the compression zone and three at the bottom for the tension. The main reinforcements were tied up with a shear link of a 2 mm-diameter steel bar at 40 mm of spacing on the beam using cable ties, as shown in Figure 6. The steels bars with 6 mm-diameter and 5 mm-diameter were used for the slab's longitudinal and transverse steel reinforcement. They were tied up with cable ties as shown in Figure 7, while Figure 8a,b presents the IBS components after casting. Also, Figure 9 shows the IBS components after casting.

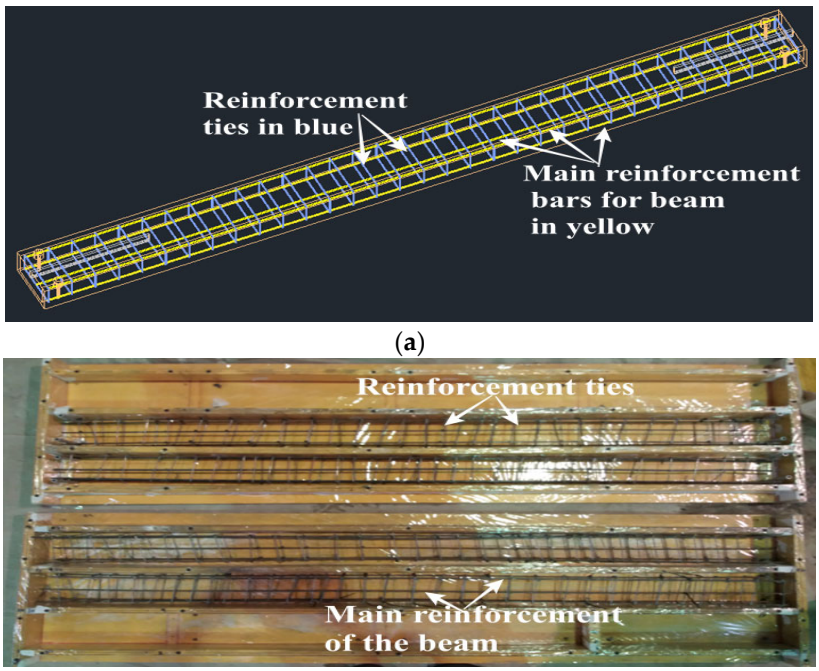

(**a**)

(**b**)

Figure 7. Details of beam reinforcement: (**a**) AutoCAD drawing; (**b**) laboratory experiment.

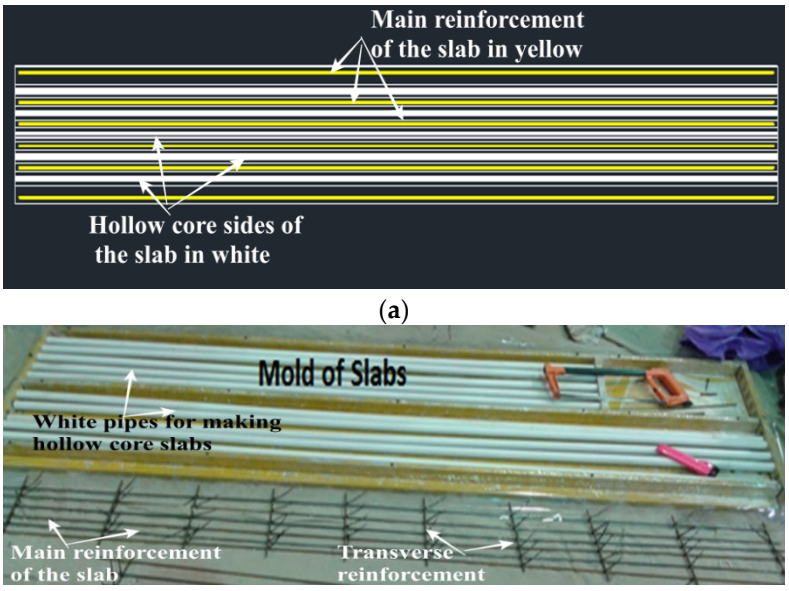

Figure 8. Details of slabs reinforcement: (**a**) AutoCAD drawing; (**b**) laboratory experiment.

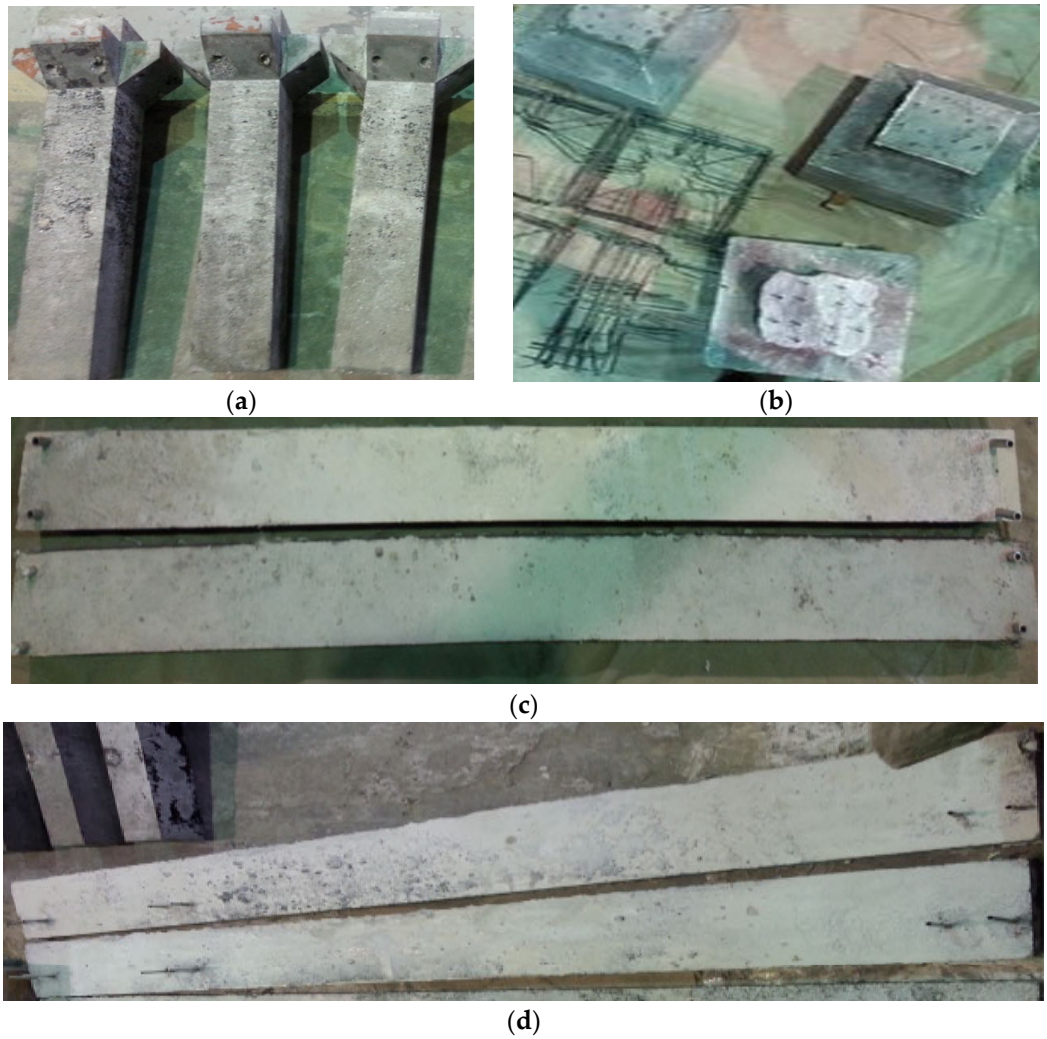

Figure 9. IBS components after casting: (**a**) columns; (**b**) hollow core footings; (**c**) beams; (**d**) slabs.

2.2.3. Design Process of Corbel and the Steel Bolts

Design of Full-Scale Corbel

The corbel of the steel-bolt-connected IBS structure is well designed using Eurocode 2 guidelines. Axial force, N_{Ed} = 651 kN.

Concrete strut

d = 500 − 40 = 460 mm
a_H = 40 mm
a_C = 150 mm
$a' = a_C + 0.2 \times a_H$
$a' = 150 + 0.2 \times 40 = 158$

$$\frac{a'}{d} = \frac{158}{460} = 0.343$$

$$f_{cd} = 0.34\left(1 - \frac{f_{ck}}{250}\right) f_{ck} = 0.34\left(1 - \frac{30}{250}\right) * 30 = 8.98\ \mathrm{N/mm^2}$$

$$\frac{F_{Ed}}{b_w * d * f_{cd}} = \frac{651}{500 * 460 * 8.98} = 0.315$$

Hence, from Table 7 (Mosley, 2010), θ = 58^°

$$z = a' \tan\theta = 158 * \tan 58^{\circ} = 253\ \mathrm{mm}$$

Main tension reinforcement

$$F'_{td} = F_{Ed}(\cot\theta + 0.2)$$

$$F'_{td} = 651(\cot 58 + 0.2) = 537\ \mathrm{kN}$$

$$A_s, \mathrm{main} = \frac{537 * 10^3}{0.87 f_{yk}} = \frac{537 * 10^3}{0.87 * 500} = 1234.5\ \mathrm{mm^2}$$

Provide = 4H20, $A_s = 1257\ \mathrm{mm^2}$.

Horizontal links

Because $\frac{a_c}{h_h} = \frac{150}{500} = 0.3 < 0.5$, closed horizontal links will be provided.

$$A_s \mathrm{link} \geq k * A_s, \mathrm{main} = 0.5 * 1235 = 618\ \mathrm{mm^2}$$

Provide 4H16, $A_s = 804\ \mathrm{mm^2}$.

Moreover, after designing the corbel, the design of column bolts using information presented by Negro [52] is followed in the next section.

Design of Steel Bolts

The steel bolts of these IBS components were designed based on the method provided by Negro [52]. The process is presented below.

$$\text{Axial force, } N_{Ed} = 651\ \mathrm{kN}$$

Materials:

Characteristics strength of concrete, f_{ck} = 30 N/mm²
Characteristics strength of steel, f_{yk} = 500 N/mm²

$$\text{Axial force, } N_{Ed} = 651\ \mathrm{kN} \quad (6)$$

Assumed: ∅_bar = 6 mm
n = number of bolts (2)
$\propto = \frac{\sigma}{f_{yk}}$ and γ_c = 1.5

$\gamma_s = 1.15$
σ = normal tensile stress due to other possible contemporary on the bolt
Assumed 325.5

$$R_d = 0.9\, n\, \emptyset^2 \sqrt{(f_{yd} * f_{cd} * (1 - \propto^2))} \quad (7)$$

$$\propto = \frac{\sigma}{f_{yk}} = \frac{325.5}{500} = 0.651 \quad (8)$$

$$f_{cd} = \frac{f_{ck}}{\gamma_c} = \frac{30}{1.5} = 20 \quad (9)$$

$$f_{yd} = \frac{500}{1.15} = 435 \quad (10)$$

$$R_d = 0.9 \times 2 \times 6^2 \times \sqrt{(435 * 20 * (1 - 0.651^2))}$$

$R_d = 4587\ N$

Beam edge

b = width of the column
C = 15 mm, edge distance of bolt
R = given force for the shear resistance of the bolt (6 kN)
h = 8 Ø, effective length of the bolt (8 × 6 = 48)

$$\beta = 0.1(\frac{\emptyset}{c})^{0.2} = 0.1(\frac{6}{15})^{0.2} = 0.083$$

$$\propto = 0.1(\frac{h}{c})^{0.5} = 0.1 * \frac{8*6}{15} = 0.32$$

$$k = \frac{b}{3C} = \frac{100}{3*15} = 2.222$$

$$\psi = 1.4\ or\ 1.0\ (EC2)$$

$$R_{Rk} = 1.4\ k\ \emptyset^{\propto} h^{\beta} \sqrt{(f_{ckcube} * C^3)}$$

$$R_{Rk} = 1.4 * 6^{0.32} * 48^{0.083} \sqrt{(30 * 15^3)} = 1289.6\ \text{N}$$

Design of Flexural Steels Bolts for Scaled-Down Structure

The flexural design of steel bolts for the downscaled IBS component was designed based on the method of Negro [52]. The process is presented below:

A_s = sectional area of the bolt = $\frac{\pi D^2}{4} = \frac{3.14 \times 6^2}{4} = 28.26$ mm²

f_{yk} = steel bolt strength (614 N/mm²)

Z = lever arm, spacing between two bolts (70 mm)

$$f_{yd} = \frac{f_{yk}}{\gamma_s} = \frac{614}{1.15} = 534\text{N/mm}^2$$

$$M_{Rd} = A_s * f_{yd} * Z \geq M$$

$$M_{Rd} = 28.26 * 534 * 70 = 1056358.8\ \text{(N mm)}$$

$$\frac{R}{R_{Rd}} \leq 1,\ R_{Rd} = \frac{R_{Rk}}{\gamma_C} = \frac{1289.6}{1.5} = 859.73\ \text{N}$$

Assumed the calculation of full scaled structural moment: M = 43.2 kN m (from multi-frame analysis),

$$A_s = \frac{\pi * 30^2}{4} = 706.9, f_{yd} = 534, Z = 70 * 5 = 350$$

$$M_{Rd} = 706.9 * 534 * 350 = 132.12 \geq M = 43.2,$$

Ok

2.2.4. Specifications of the IBS Frame

The dimensions of all components, including hollow-core footings, columns, beams, and hollow-core slabs, were scaled down according to their original dimensions. The steel-bolt-connected IBS frame consists of three column-footing structures with the same dimensions as those shown in Figure 10a–e, which were used to form the structure.

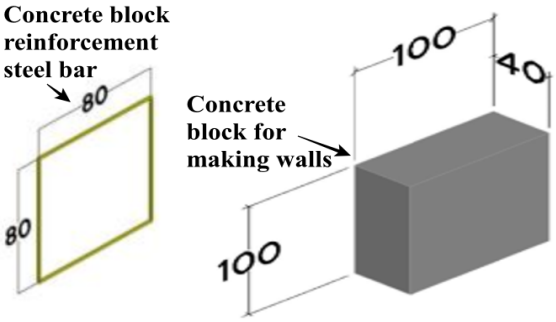

(**a**)

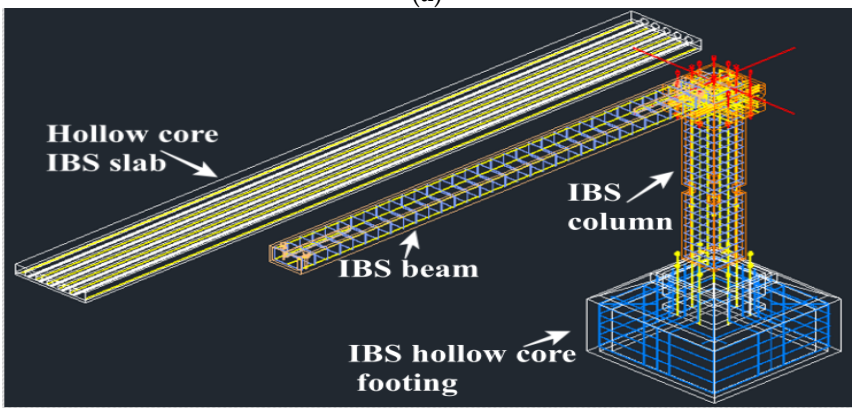

(**b**)

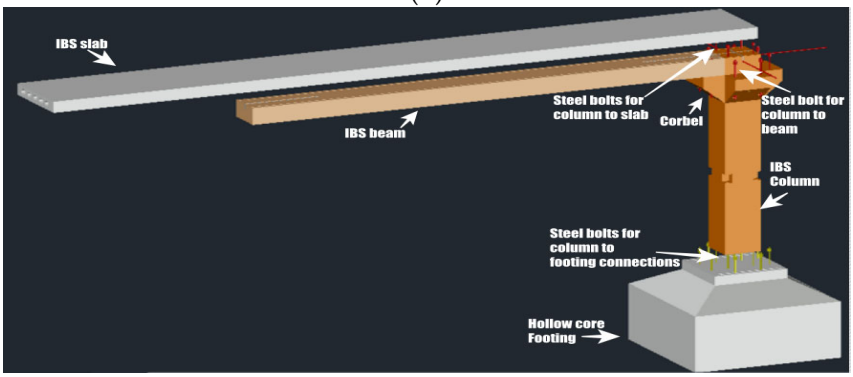

(**c**)

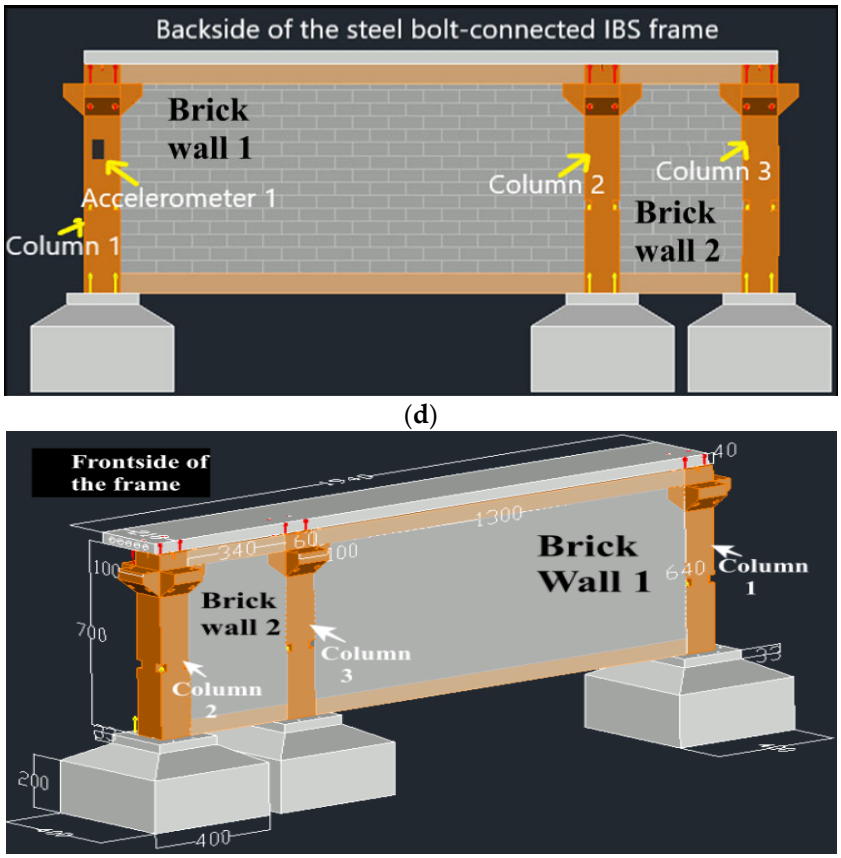

Figure 10. IBS frame: (**a**) details of brick; (**b**) AutoCAD reinforcement details; (**c**) frame components; (**d**) back of the frame; (**e**) front of the frame.

Four beams with two different dimensions were connected to the footings and columns corbels: 1300 mm length × 100 mm breadth × 60 mm thickness; 340 mm length × 100 mm breadth × 60 mm thickness. The dimensions of the hollow-core slab are 1940 mm length × 220 mm breadth × 40 mm height, as shown in Figure 10d. There are two infill walls in the frame which were made up of concrete blocks as the bricks with the dimension of 100 mm × 100 mm × 40 mm. The first infill wall from the left side in Figure 10d covered the area of 1300 mm × 580 mm with a thickness of 100 mm, and the total brick blocks are 183. The second infill wall covered the area of 340 mm × 580 mm with a thickness of 100 mm and 35 total blocks.

2.3. Procedure of Autodesk CFD Simulation for IBS Frame

The process was started by importing the AutoCAD drawing of the testing tank with the modeling inside it. Figure 8 shows the reservoir on the right side filled with water as number 1, while the left side region where the modeling was placed is marked as number 2. The reservoirs were separated by a retaining wall with a gate cutout to allow water to pass between. Regarding the material properties, concrete material was assigned to the slabs, beams, columns, and hollow-core footings. Water was assigned to both reservoirs (1 and 2). Since Reservoir 1 was filled with water to flow to Reservoir 2, the height of fluid (HOF) initial condition was applied to Reservoir 1. The pressure condition was automatically applied at the liquid–air interface. Thus, there was no need to apply an additional pressure of boundary conditions in this model. Figure 11 presents the testing process.

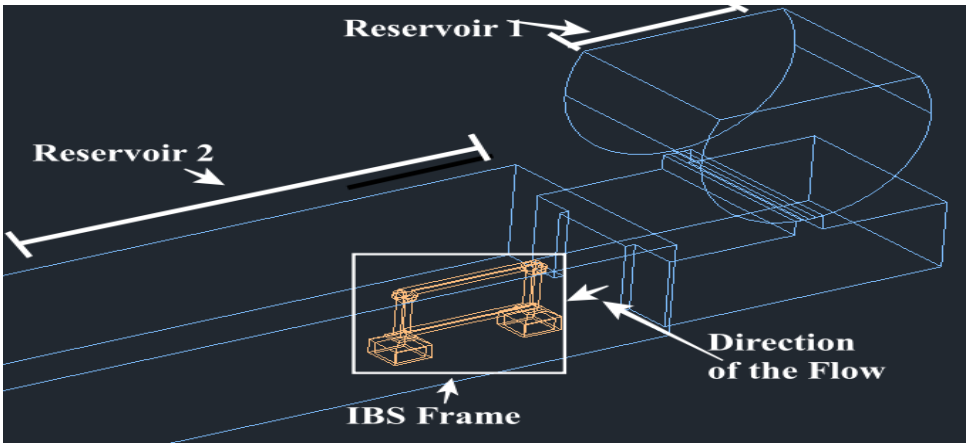

Figure 11. The testing tank with the model.

The meshing size for this project was set to be automatic during the simulation, but refining the meshing might take place at the condition where the air and water interact. After completing the meshing process, the next step was to click on the "Solve" or "Run" menu, but before clicking "Solve", the following steps must be conducted as follows:

- On the physics tab of the "Solve" dialog, click "Free Surface" and check it to enable the free surface.
- Specify a gravity vector: In this case, gravity acts in the –Z-axis direction, so set the Earth gravity directional unit vector to 0,0, −1.
- The "Solution Mode" is automatically set to "Transient" on the "Control" tab, and the "Time Step Size" is automatically set to 0.01.
- To animate the results, a value needs to be specified for "Save Intervals" > "Results".
- Specify the number of time steps (8000 were used for this IBS frame simulation), and click "Solve".

Hence, in order to view the fluid flow after finishing solving the model, the following steps have to be followed: right-click the model and then click select "Free Surface". To animate the filling process, right-click the model and animation; on the "Animation" dialog, click "Animate", and then the "Play" button.

3. Results, Analysis, and Discussions

3.1. CFD Simulation of IBS 2D Frame

The pressure was used as the substitute to assign the flooding load forces. The water was released, and then the pressure directly impacted the IBS structure, as shown in Figure 12a. It was found that the maximum pressure occurs at the impact area on the column–footing connection and the bottom side beam as well. The other part of the structure suffered from the vibration impact, which is part of the investigation to observe the resistance of vibration by the structure. Additionally, Figure 12a shows the pressure and the velocity around the IBS frame from the contour tables as 20,000 Pa and 1500 cm/s, respectively, while Figure 12b,c show the graphs of velocity and pressure at the time of running the simulation model. The maximum velocity and pressure from the graphs were recorded as 8.96×10^3 cm/s and 2.59×10^7 Pa, respectively. The maximum velocity and pressure from the graphs are not necessarily from the surrounding area of the 2D frame. The graphs captured the maximum rate, while the contour (Figure 12a) provides the maximum values and the exact velocities and pressures around the structures. The software simulations served as the guideline for the experimental work. The numerical simulations worked very well, provided a good result, and showed the performance behavior of the structures. This is usually the case when the components of the CFD simulation, fluid domain, meshing, and boundary condition are properly controlled;

hence, leading to accurate results from the CFD [53]. Table 9 presents the pressure and velocity results of the simulated CFD for both graphs and contour.

Table 9. Simulation CFD results for the IBS frame.

Parameters	Results of Contour at the Model	Maximum CFD for Frame	
		Contour	Graph
Velocity (m/s)	17.5	88.77	89.58
Pressure N/mm²	0.40	1.58	25.91

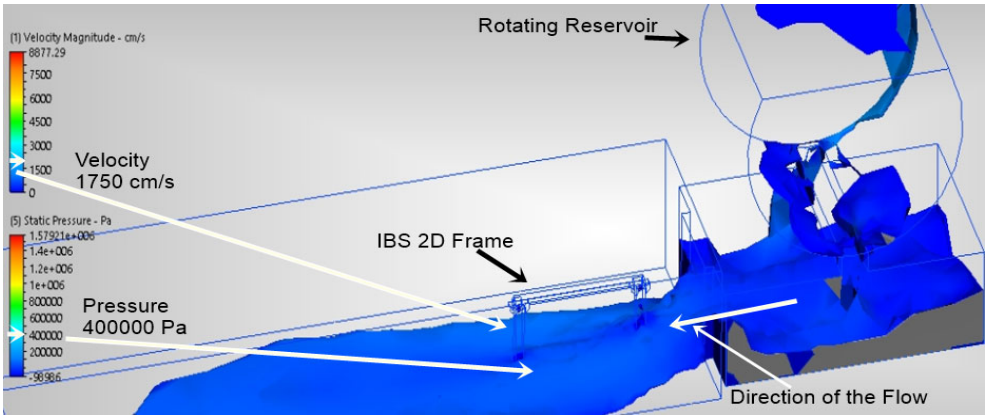

(**a**)

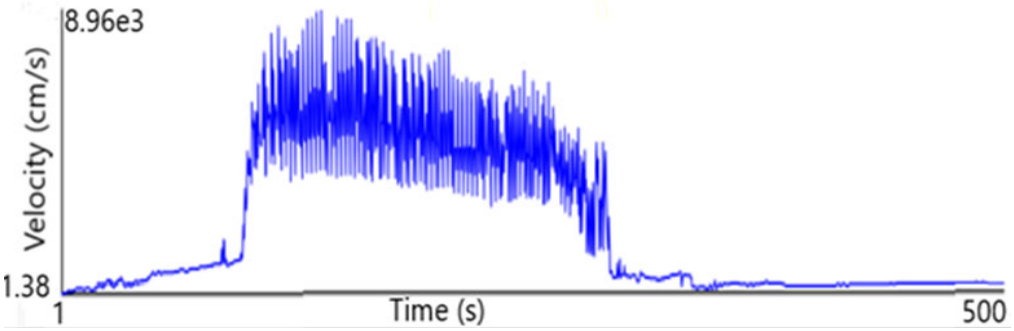

(**b**)

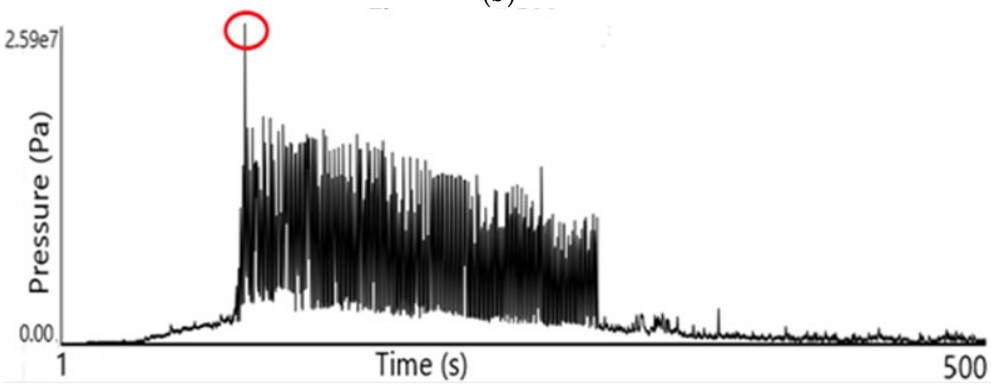

(**c**)

Figure 12. Illustrations of the CFD results for 2D frame: (**a**) simulated fluid flow; (**b**) maximum velocity; (**c**) maximum pressure.

3.2. Experimental Dam-Break Test of the IBS Frame

After fabricating the IBS model components in the laboratory, the components were assembled in the testing dam-break at the deck's specific position, which is 1370 mm away from the pond area inside the dam-break tank. The ponded area was measured at

2440 mm × 2000 mm × 300 mm. A pressure meter is an instrument that was used to detect external load or pressure. Eight waterproof pressure meters were installed at specified locations in front of the IBS frame model for measuring hydrodynamic impact pressure. One load cell was installed at the top of the frame by tightening it with the bolt to record the vibration of the column bolt. Three accelerometers were used on the frame to record accelerations and displacements in the direction of the flow, respectively. Figure 13a–c display the exact positions of the instruments.

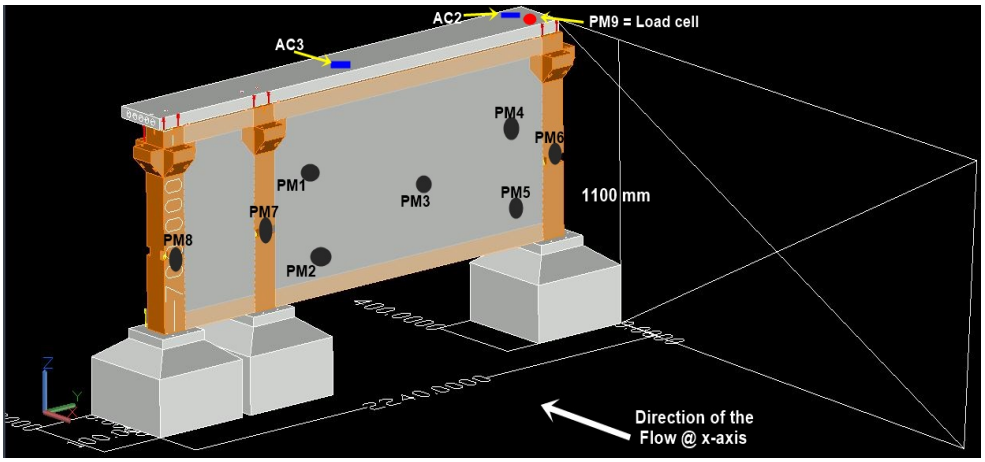

(**a**)

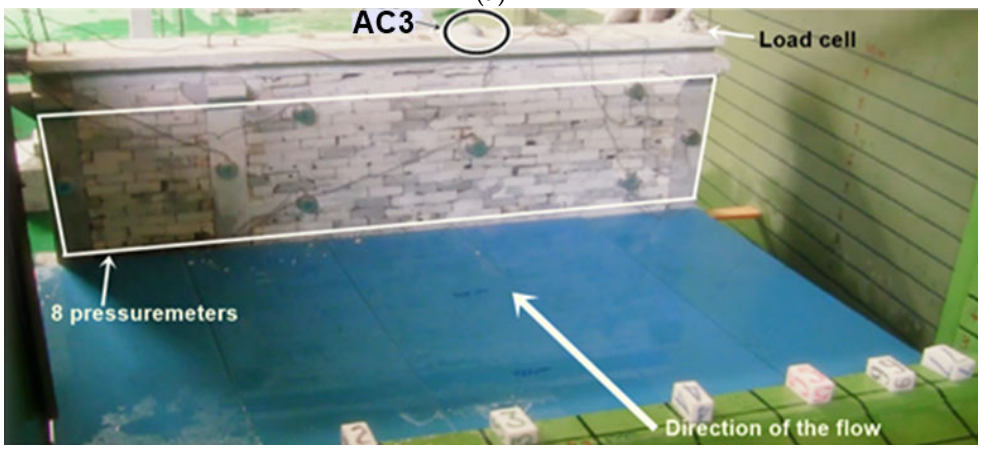

(**b**)

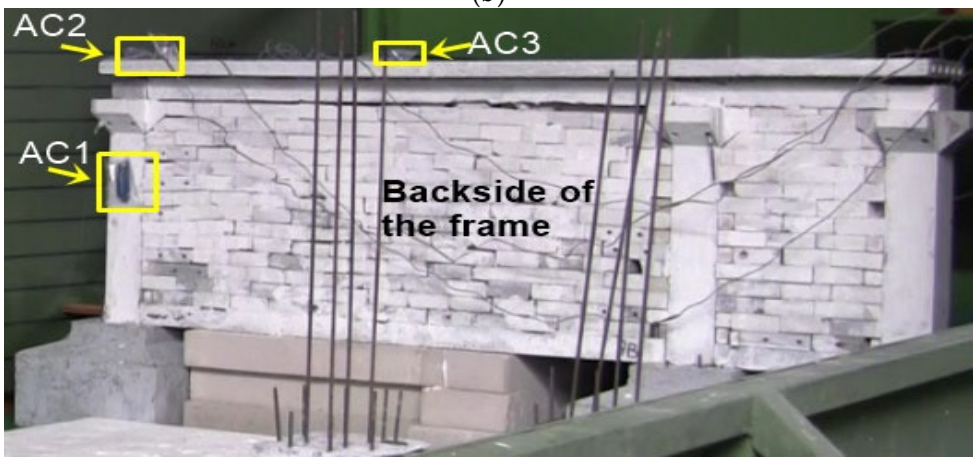

(**c**)

Figure 13. IBS frame ready for testing: (**a**) schematic diagram; (**b**) front of the experimental test; (**c**) back of the frame.

All pressure meters and load cell sensor measurements were connected to a data logger to record a continuous time history response during the test. The rotating tank was locked while the opening gate was at the top position to fill in the tank with water to a target height. The sport light for video camera visibility was set at a position above the tank to record the model's movement due to water splash. Then, the motorized torsional derive was switched on to allow the water tank to rotate clockwise; the water flowed downstream as a hydraulic bore pressure against the structure.

3.2.1. IBS Frame Test 1 for 1 m Reservoir Water Level

Figure 14 shows the first test of the frame, which was conducted using 1 m reservoir water level. The horizontal hydrodynamic force was subjected to the structure for investigating the behavior of the IBS frame structure.

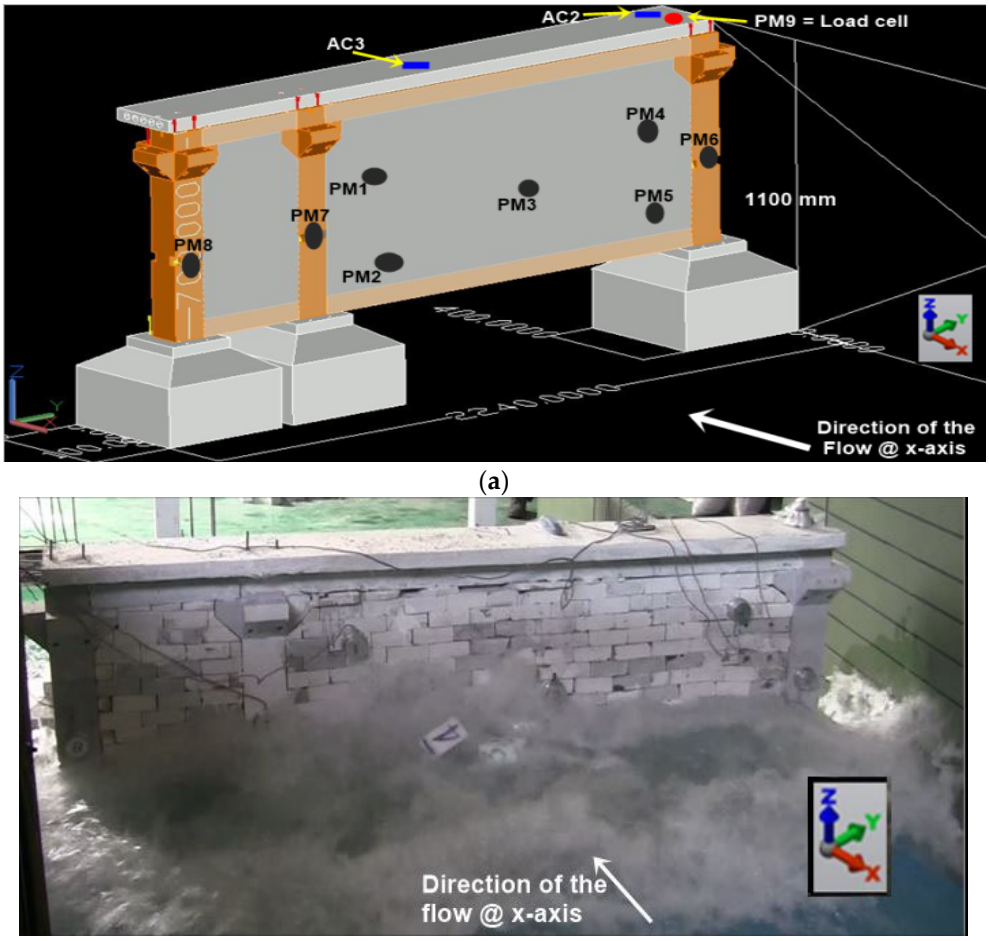

Figure 14. Dam-break test for 1 m reservoir water level: (**a**) schematic diagram of the dam-break test: (**b**) during test 1 of 2D frame.

The test lasted up to 13 s from the beginning to the end. In the first 3 s, the hydraulic jump rebounded height reached the height of the slab. During this test, all eight PMs detected the forces that impacted the front surface of the frame. When the test reached 12–13 s, the bore flow around the structure dropped drastically and dissipated. Among the nine PMs, PM5 measured the highest force value as 13.75 kN. The distance between PM5 and the floor deck was 20 cm. Due to the closeness of PM5 to the floor deck, there was a possibility for detecting a high impact force because of the sudden impact of hydrodynamic force at the area. PM9 was used to measure the vibration of the bolt connected to the slab, column, and the footing at any little deflection. PM9 did not detect any

value during this test due to the low impact of hydrodynamic force on the structure; Figure 15 shows the graph. The height of the water on the structure after the hydraulic impact reached a 40 cm height, and the total water volume that impacted the structure was around 3.15 m^3.

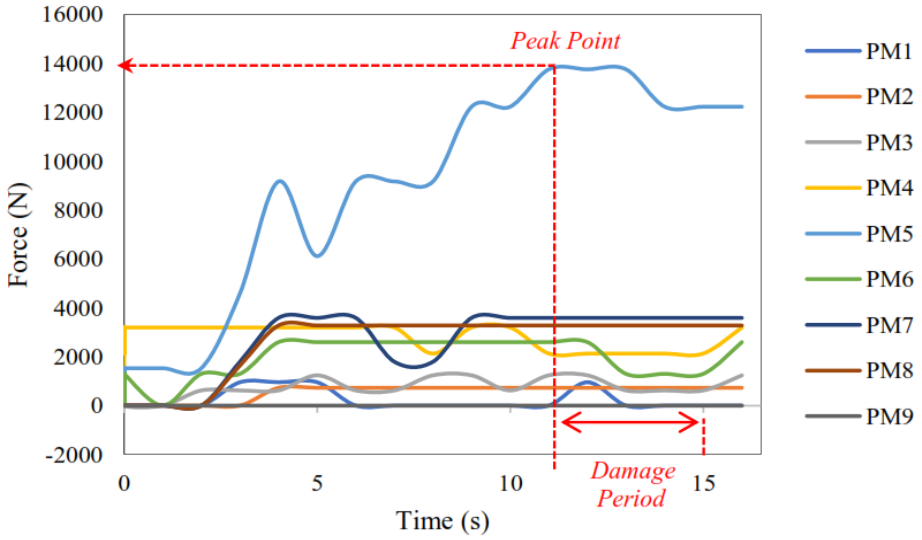

Figure 15. Graph of 1 m reservoir water level test of the frame.

3.2.2. IBS Frame Test 2 for 2 m Reservoir Water Level

The second test on the same IBS frame was conducted according to the first test. The reservoir water height of 2 m was used for furthering the investigation to acquire more information about the impact of hydrodynamic force on the frame. In the first 3 s of the test, the hydrodynamic force reached the structure, and the hydraulic jump spread to the whole front face of the frame. After 6 s of the test, the hydrodynamic force increased against the frame, and it deflected backward due to the increases in the hydrodynamic forces. Figure 16a,b show the structures after 6 s from the start of the test. The height of the water reached 50 cm on the frame, and the total volume that impacted the structure was around 3.94 m^3.

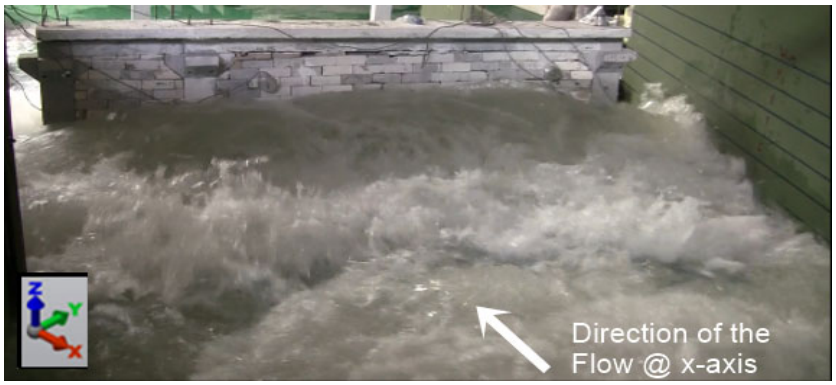

(**a**)

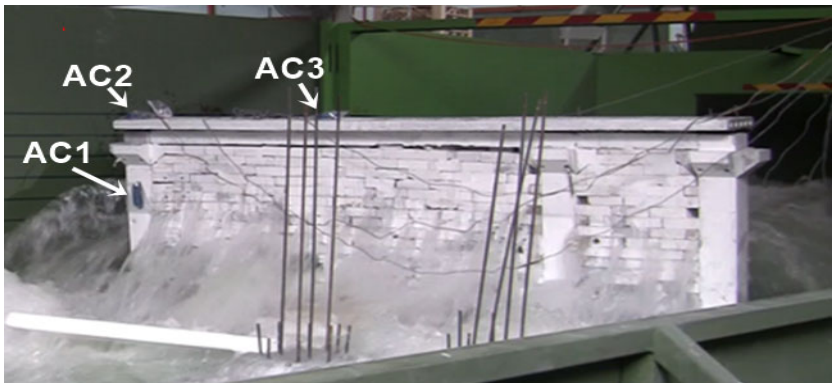

(**b**)

Figure 16. Dam-break test 2 for 2 m reservoir water level: (**a**) front of the frame; (**b**) back of the IBS frame.

After the dissipation of the impounded water from the surrounding area of the frame, the damages to the brick walls were clearly visible. It can be seen that the 2 m impounded water depth caused a higher impact on the structure than the 1 m impounded water depth. Figure 17 displays the damaged areas on the brick walls.

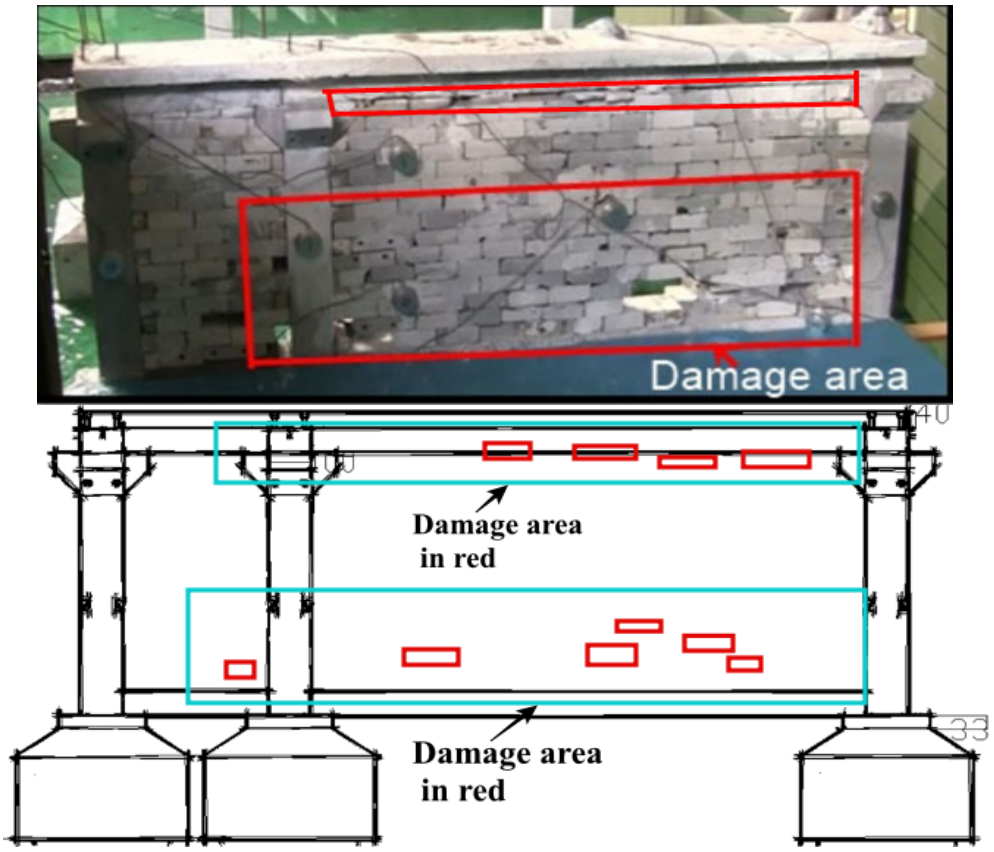

Figure 17. Damages of the frame after the Test 2.

During this test of 2 m impoundment water depth, all the pressure meters detected the impact of hydrodynamic forces on the structure. PM5 detected the highest impact (58.01 kN) after 8 s, followed by PM9, with a recorded value of 37.41 kN after 6 s of the test. PM9 was used to detect the vibration of the bolt during the deflection of the structure. The structure was deflected because of the high impact of hydrodynamic forces. Figure 18 illustrates the graph of the test results.

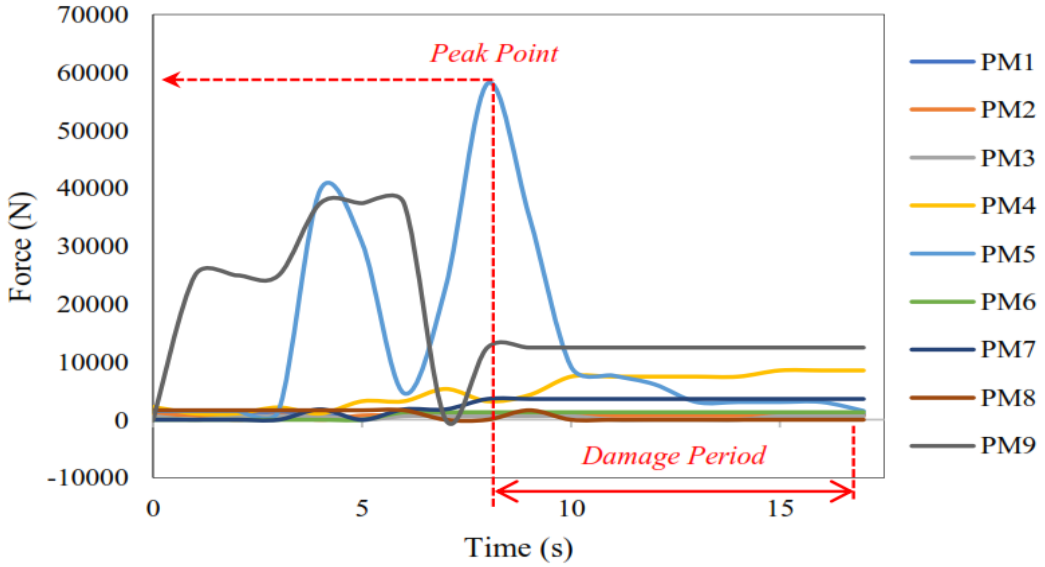

Figure 18. Graph of 2 m reservoir water level test for the frame.

3.2.3. IBS Frame Test 3 for 3 m Reservoir Water Level

The third serial test of the 2D frame was conducted using 3 m impounded water depth, and the test lasted for about 17 s. In the first 7 s of the test, the frame structure deflected backward because of the high pressure from hydrodynamic forces which flowed against the structure. Figure 19a shows the front side of the structure during the test, while Figure 19b presents the back at the time of deflection. The severely damaged walls are presented in Figure 19c; the walls were damaged because of the hydrodynamic force that impacted the frame. The height of the water that impacted the structure was about 70 cm. The total volume of the water that caused the damage to the structure was around 5.52 m^3.

Eight pressure meters (PMs) were attached to the frame's front surface to measure the applied hydrodynamic force on the structure. One pressure meter (PM9) was attached to the column's bolt to measure the structure's deflection. PM9 recorded the data of the through-bolt vibration when the structure deflected during the test. After completing the test, PM9 measured the highest value among the PMs because of the high deflections of the structure. The highest value (62.34 kN) was recorded by PM9 after 7 s, followed by PM4, with a value of 34.06 kN after 7 s. Figure 20 illustrates the graph of the results.

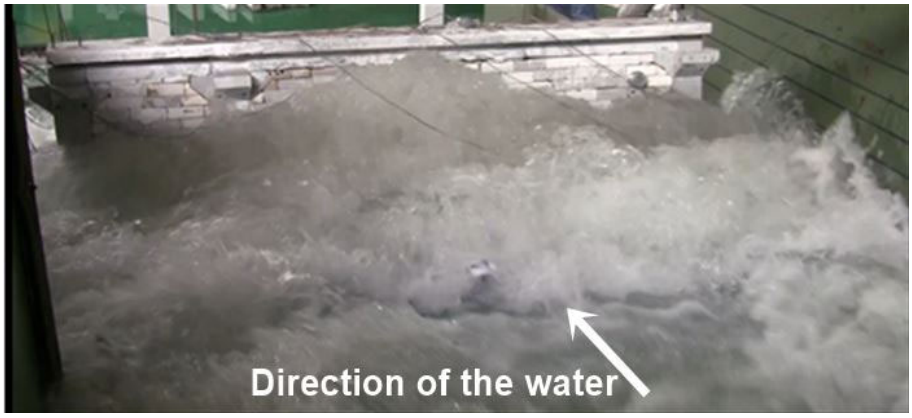

(**a**)

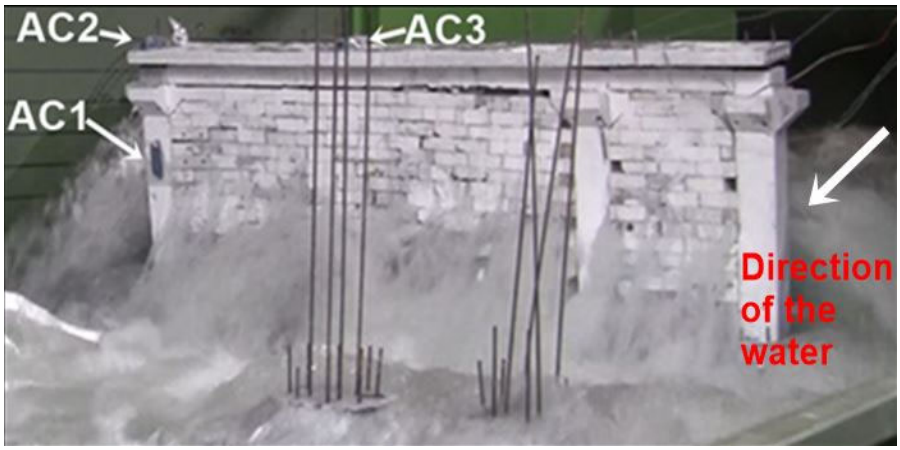

(**b**)

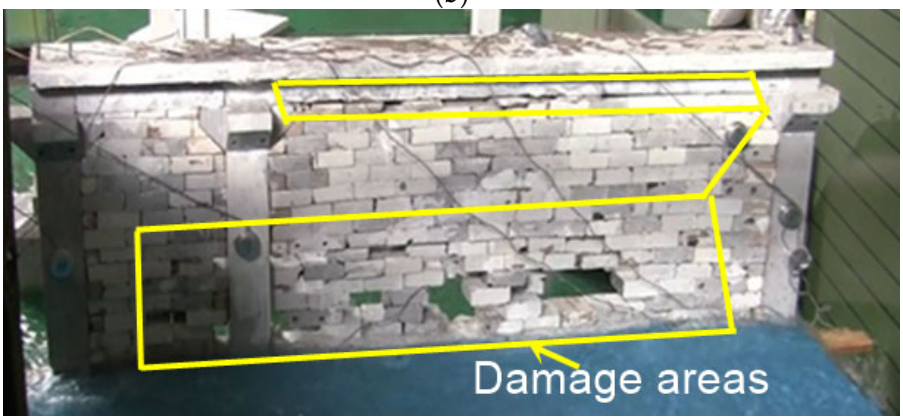

(**c**)

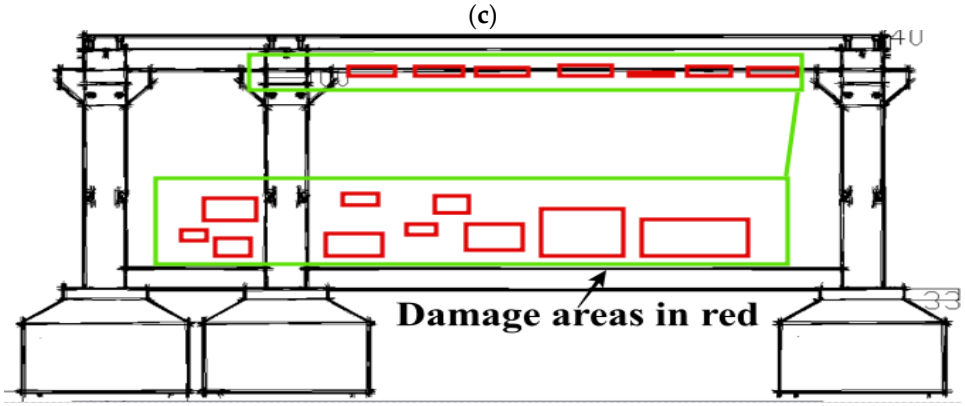

(**d**)

Figure 19. Dam-break test 3 for 3 m reservoir water level: (**a**) front of the frame during the test; (**b**) back of the frame during the test; (**c**) damage to the frame after test 3; (**d**) sketch of the damages.

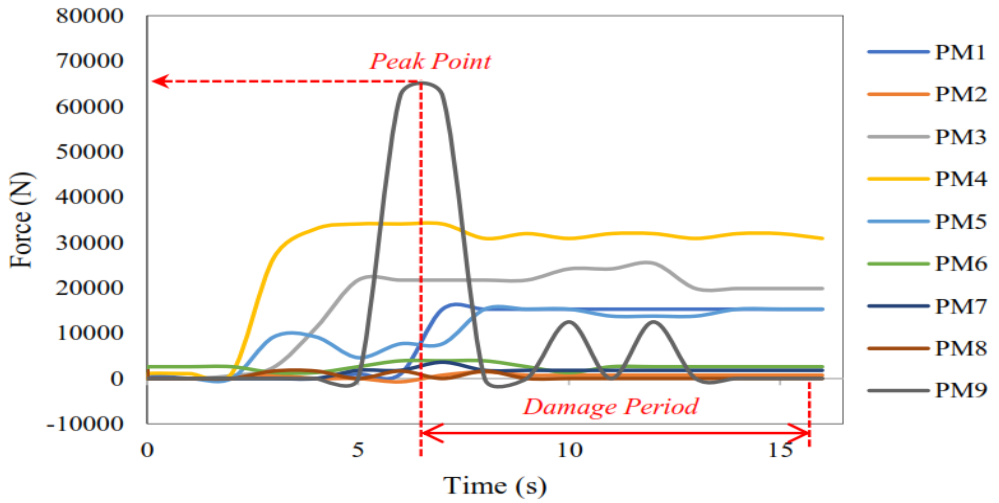

Figure 20. Graph of 3 m reservoir water level test 3 for model 2.

3.3. Dynamic Properties

Three dam-break tests were conducted on the IBS frame to obtain the dynamic properties of the structure. The vibration data were recorded using three accelerometers. They were analyzed using seismosignal to identify the frequency and period. The results of the dynamic properties of the frame structure were presented in Tables 10–12, respectively.

Table 10. Dynamic properties of the IBS frame for test 1.

Accelerometers	Frequency (Hz)	Period (s)	Displacement from ACs (cm)
AC1	8.11	0.12	0.14
AC2	14.84	0.07	2.53
AC3	12.50	0.08	1.97

Table 11. Dynamic properties of the IBS frame for test 2.

Accelerometers	Frequency (Hz)	Period (s)	Displacement from ACs (cm)
AC1	0.78	1.28	27.42
AC2	0.98	1.02	21.34
AC3	0.98	1.02	22.41

Table 12. Dynamic properties of the IBS frame for test 3.

Accelerometers	Frequency (Hz)	Period (s)	Displacement from ACs (cm)
AC1	8.11	1.46	46.97
AC2	0.68	1.46	53.74
AC3	0.71	1.51	54.12

The seismosignal was used for analyzing the recorded data of accelerometers for the test of 1 m, 2 m, and 3 m reservoir water depth. Figure 21 shows the positions of the accelerometers on the frame. Figure 22 presents the time histories recorded during the IBS frame's dam-break test. These histories are based on the highest acceleration generated by the sudden impact of hydrodynamic forces against the structural frame.

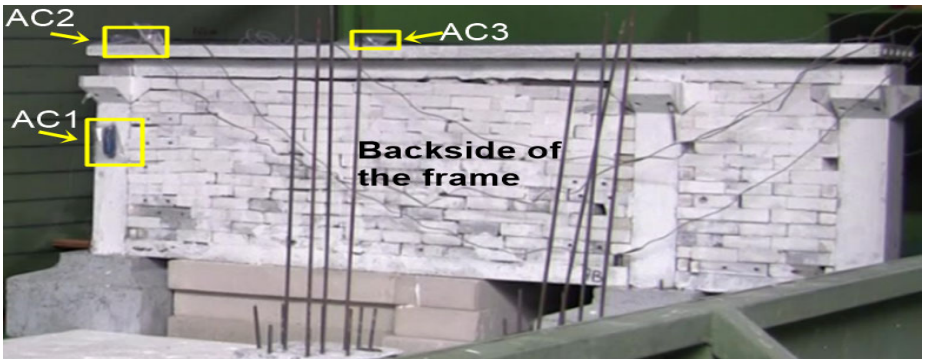

Figure 21. Illustrating the positions of the accelerometers of the height of the frame.

The maximum accelerations, which were recorded using three different accelerometers during the tests, were analyzed using seismosignal to understand the frame structure's behavior. During the third dam-break test of the IBS frame, the accelerometers recorded the highest acceleration due to the high impact of hydrodynamic forces against the structure. Table 13 presents the results of the maximum acceleration for the 2D frame.

Table 13. Peak values of accelerations for the IBS frame.

Accelerometers	Peak Accelerations (m/s²)		
	1 m Reservoir Water Height	2 m Reservoir Water Height	3 m Reservoir Water Height
AC1	0.012	0.080	0.170
AC2	0.014	0.070	0.100
AC3	0.013	0.050	0.090

The purpose of using accelerometers on this IBS frame was to detect and measure any vibration or acceleration motion of the bolt-connected IBS frame structure during the tests. Therefore, Table 14 shows the maximum accelerations for the steel-bolt-connected IBS frame which were recorded by three accelerometers during the dam-break tests. In the first, second, and third tests, the edge of the slab from the side of column 1 experienced the highest acceleration of 0.01446 g, 0.07609 g, and 0.16797 g, respectively, and AC2 and AC1 recorded them. The minimum acceleration for the first, second, and third tests were 0.01279 g, 0.05129 g, and 0.08524 g, respectively, and they were all recorded by AC3. AC3 was located at the mid-point of the slab, an area which is highly likely to resist low acceleration due to the dissipations of the hydrodynamic forces. By the time the frame deflected a bit during test 2 and test 3, the edge of the frame where AC2 was located was more likely to detect a higher vibration than the middle of the slab due to the edges of the frame experiencing high impacts of the hydrodynamic force when the water was passing from the edge of column 1. AC1 recorded the highest acceleration of the frame, since AC1 was placed at the back of column 1. Column 1 experienced the highest vibrations due to the deflection of the frame during test 2 and test 3. Hence, the steel bolt connection showed a durable performance, which made the connections of the IBS frame more ductile and able to withstand the high horizontal impact of the flood. Finally, the steel-bolt-connected IBS frame was designed to resist the high impact of hydrodynamic force based on the FEMA P-646 [54], FEMA P-55 [55], and Aghl [56] design methods, while the steel bolt was designed based on Negro [52] method.

Table 14. Comparison between dam-break and CFD results for IBS frame.

Parameters	Experimental Results	Results of Contour at the Model Side	Maximum CFD for Frame	
			Contour	Graph
Velocity (m/s)	7.67	17.5	88.77	89.58
Pressure (N/mm²)	31.75	0.40	1.58	25.91

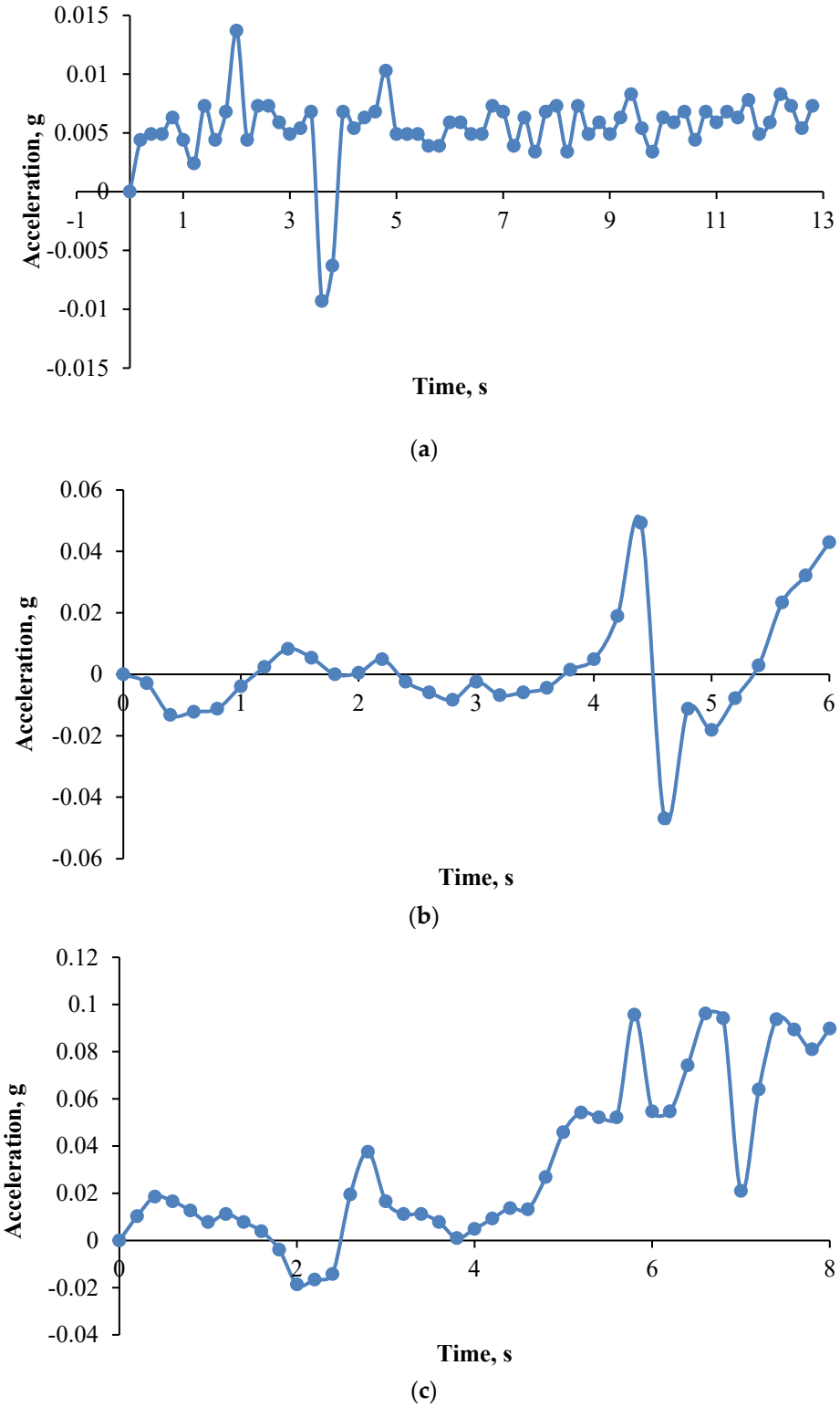

Figure 22. The maximum acceleration from AC3 for: (**a**) test 1 with 1 m water level; (**b**) test 2 with 2 m water level; (**c**) test 3 with 3 m water level.

3.4. Comparison of Dam-Break Tests with CFD Simulation

The pressure and velocity results of the frame for both the CFD simulation and the laboratory experiment were compared, as shown in Table 14. The purpose of CFD simulation in this research was to provide a very good assumption for the parameters that would be used for conducting the laboratory experiment. The maximum value of velocity

from the contour and the maximum value of velocity from the graph were compared with the experimental results and the results around the model from the contour. The maximum velocity value from the graph was higher than the result of velocity from the contour and the experimental work. Additionally, the experimental result of velocity was less than the maximum result of velocity from the contour due to the assumed applied pressure during the simulation or due to some issues related to the meshing. The lesser the size of the meshing, the better the results, but it needs a high-speed processor and time.

Furthermore, the experimental result of the pressure was higher than the results of CFD for both the contour and the graph. The CFD simulation was simulated properly, and the fluid domain, meshing, and boundary conditions were carefully controlled appropriately, leading to this accurate simulation. Comparing the results of the CFD from the contour with the results of the CFD graph showed the accuracy of the simulation because they have a reasonable result, which proves their good agreement, and the percentage difference between the maximum velocities for both contour and graph was 0.9% (Table 14). Moreover, the fluid flows for CFD in Figure 12a correspond to the experimental fluid flows in Figures 14b, 16a, and 19a. The pressure impact for CFD on the graph in Figure 12c corresponds precisely to the pressure graphs depicted in Figures 15, 18, and 20 for the experimental test. The CFD simulation predicted the experimental dam-break test properly, and it also provided a very good guideline for the experimental work. However, the experimental results represent the real behavior of the model under the laboratory test. The CFD simulation was made earlier, before the experimental work, and it helped in carrying out the experimental work successfully.

4. Conclusions

Computational fluid dynamic (CFD) simulation software was used to predict the optimized design, performance, and behavior of the 1:5 downscaled IBS frame model before manufacturing it in the laboratory and transferring it to the testing place. A two-dimensional bolt-connected IBS frame model was successfully simulated using Autodesk CFD for investigating the behavior of steel-bolt-connected IBS structural models to optimize the experimental dam-break test. In this CFD analysis, an examination of fluid flow's physical properties, such as velocity and pressure, was conducted to investigate the performance of the 2D frame. After the simulation, velocity and pressure results were obtained from the contour and the graph for the IBS frame. Both the graph and the contour provide very good results which were very close to each other (graph and contour). This showed a very good agreement between both results. The results of the CFD simulations were compared to the experimental results, which showed some differences. Velocities from the CFD were higher than the experimental velocities, which were calculated using the Bernoulli equation, whereas the experimental result of pressure was higher than the CFD results for pressure from both the graph and the contour. Based on the major findings of this research, several conclusion points were drawn as follows:

- Based on the literature reviews, it was found that there are several parts of flood-prone zone structures which include commercial buildings, residential buildings, and schools, which have been destroyed during flooding events. Those structures mostly comprised conventional building systems. Hence, it is important to consider other building systems, which can limit costs, speed up the building process, and reduce the construction risk, while being robust and durable.
- The experimental dam-break tests of the IBS frame showed that the steel bolt connection had very good strength.
- This model recorded the highest hydrodynamic force of 62.3 kN, and the structure neither failed nor showed signs of being broken in the bolt after the test. Hence, the bolt has met our expectations, and it can be practically used in real structural con-

nections due to its ability to resist high-impact pressure, mainly because of its strength and ductility performance.

- This steel-bolt-connected IBS satisfied the mentioned qualities. This 1:5 downscaled IBS frame resisted the maximum horizontal force of 62.3 kN, showing its capability to perform well in an earthquake zone, satisfying the seismic design.
- The steel-bolt-connected IBS frame was designed to resist the high-impact hydrodynamic force; therefore, the implementation of this innovated steel-bolt-connected IBS in flood-prone zones will be feasible and helpful for both inhabitants and their governments.
- The CFD simulation predicted the experimental dam-break test properly and it also provided a very good guideline for the experimental work. However, only the experimental results represented the real behavior of the model under the laboratory test. The CFD simulation was made before the experimental work, and it successfully helped in carrying out the experimental work.
- Advantages of this proposed steel bolt connection over conventional construction methods and other IBS methods include the following: steel bolt connection stops failure or cracks spreading from one component to another due to energy dissipation; the failure of one component will not cause a complete collapse of the building; it provides additional strength and ductile behavior for the structures; it would make structures more reliable throughout their lifespans compared with conventional methods of construction.

Author Contributions: Conceptualization, A.S.A., N.M.N., M.S.A.S., and S.U.; data curation, A.S.A., N.M.N., M.S.A.S., S.U., M.A. (Mugahed Amran), M.A. (Musa Adamu), N.I.V., and R.F.; formal analysis, A.S.A., N.M.N., M.S.A.S., S.U., M.A. (Mugahed Amran), M.A. (Musa Adamu), N.I.V., and R.F.; funding acquisition, N.I.V.; investigation, A.S.A., M.S.A.S., and M.A. (Mugahed Amran); methodology, A.S.A., M.S.A.S., and S.U.; project administration, N.M.N.; resources, M.A. (Mugahed Amran), M.A. (Musa Adamu), N.I.V., and R.F.; software, A.S.A.; supervision, N.M.N., M.S.A.S., and S.U.; validation, N.M.N., S.U., M.A. (Mugahed Amran), M.A. (Musa Adamu), N.I.V., and R.F.; visualization, M.S.A.S., M.A. (Mugahed Amran), and R.F.; writing—original draft preparation, A.S.A.; writing—review and editing, N.M.N., M.S.A.S., S.U., M.A. (Mugahed Amran), M.A. (Musa Adamu), N.I.V., and R.F. All authors have read and agreed to the published version of the manuscript.

Funding: The research is partially funded by the Ministry of Science and Higher Education of the Russian Federation under the strategic academic leadership program 'Priority 2030' (Agreement 075-15-2021-1333 dated 30.09.2021).

Institutional Review Board Statement: Not applicable.

Informed Consent Statement: Not applicable.

Data Availability Statement: Data sharing not applicable.

Acknowledgments: The authors offer their gratitude to Alkali Mahiru Sharif Bala, and Abdul Kadir Marsono at the School of Civil Engineering, Faculty of Engineering, Universiti Teknologi Malaysia, Johor Bahru, Malaysia. Additionally, the authors gratefully acknowledge the financial support given by Deanship of Scientific Research at Prince Sattam bin Abdulaziz University, Alkharj, Saudi Arabia, Yemen, for this research.

Conflicts of Interest: The authors declare no conflict of interest.

References

1. Mohamad Yusoff, I.; Ramli, A.; Mhd Alkasirah, N.A.; Mohd Nasir, N. Exploring the managing of flood disaster: A Malaysian perspective. *Malays. J. Soc. Space* **2018**, *14*, 24–36. https://doi.org/10.17576/geo-2018-1403-03.
2. Islam, M.M.; Ujiie, K.; Noguchi, R.; Ahamed, T. Flash flood-induced vulnerability and need assessment of wetlands using remote sensing, GIS, and econometric models. *Remote Sens. Appl. Soc. Environ.* **2022**, *25*, 100692. https://doi.org/10.1016/j.rsase.2021.100692.
3. Daramola, S.; Li, H.; Omonigbehin, O.; Faruwa, A.; Gong, Z. Recent retreat and flood dominant areas along the muddy Mahin coastline of Ilaje, Nigeria. *Reg. Stud. Mar. Sci.* **2022**, *52*, 102272. https://doi.org/10.1016/j.rsma.2022.102272.
4. Menne, B.; Murray, V. *Floods in the WHO European Region: Health Effects and Their Prevention*; WHO Regional Office for Europe: Copenhagen, Denmark, 2013.

5. Chen, C.; Jiang, J.; Liao, Z.; Zhou, Y.; Wang, H.; Pei, Q. A short-term flood prediction based on spatial deep learning network: A case study for Xi County, China. *J. Hydrol.* **2022**, *607*, 127535. https://doi.org/10.1016/j.jhydrol.2022.127535.
6. Chen, M.; Papadikis, K.; Jun, C. An investigation on the non-stationarity of flood frequency across the UK. *J. Hydrol.* **2021**, *597*, 126309. https://doi.org/10.1016/j.jhydrol.2021.126309.
7. Fernando, N.S.; Shrestha, S.; KC, S.; Mohanasundaram, S. Investigating major causes of extreme floods using global datasets: A case of Nepal, USA & Thailand. *Prog. Disaster Sci.* **2022**, *13*, 100212. https://doi.org/10.1016/j.pdisas.2021.100212.
8. Bucherie, A.; Hultquist, C.; Adamo, S.; Neely, C.; Ayala, F.; Bazo, J.; Kruczkiewicz, A. A comparison of social vulnerability indices specific to flooding in Ecuador: Principal component analysis (PCA) and expert knowledge. *Int. J. Disaster Risk Reduct.* **2022**, *73*, 102897. https://doi.org/10.1016/j.ijdrr.2022.102897.
9. DID. *Urban Storm Water Management Manual for Malaysia;* Stormwater Management Division Drainage and Irrigation Department of Malaysia: Kuala Lumpur, Malaysia, 2000.
10. Membele, G.M.; Naidu, M.; Mutanga, O. Examining flood vulnerability mapping approaches in developing countries: A scoping review. *Int. J. Disaster Risk Reduct.* **2022**, *69*, 102766. https://doi.org/10.1016/j.ijdrr.2021.102766.
11. Ouma, Y.O.; Tateishi, R. Urban flood vulnerability and risk mapping using integrated multi-parametric AHP and GIS: Methodological overview and case study assessment. *Water* **2014**, *6*, 1515–1545. https://doi.org/10.3390/w6061515.
12. Jonkman, S.N.; Dawson, R.J. Issues and challenges in flood risk management-Editorial for the special issue on flood risk management. *Water* **2012**, *4*, 785–792. https://doi.org/10.3390/w4040785.
13. Chan, S.W.; Abid, S.K.; Sulaiman, N.; Nazir, U.; Azam, K. A systematic review of the flood vulnerability using geographic information system. *Heliyon* **2022**, *8*, e09075. https://doi.org/10.1016/j.heliyon.2022.e09075.
14. Hong, H.; Panahi, M.; Shirzadi, A.; Ma, T.; Liu, J.; Zhu, A.X.; Chen, W.; Kougias, I.; Kazakis, N. Flood susceptibility assessment in Hengfeng area coupling adaptive neuro-fuzzy inference system with genetic algorithm and differential evolution. *Sci. Total Environ.* **2018**, *621*, 1124–1141. https://doi.org/10.1016/j.scitotenv.2017.10.114.
15. Chen, W.; Hong, H.; Li, S.; Shahabi, H.; Wang, Y.; Wang, X.; Ahmad, B. Bin Flood susceptibility modelling using novel hybrid approach of reduced-error pruning trees with bagging and random subspace ensembles. *J. Hydrol.* **2019**, *575*, 864–873. https://doi.org/10.1016/j.jhydrol.2019.05.089.
16. Murali, G.; Abid, S.R.; Amran, M.; Fediuk, R.; Vatin, N.; Karelina, M. Combined Effect of Multi-Walled Carbon Nanotubes, Steel Fibre and Glass Fibre Mesh on Novel Two-Stage Expanded Clay Aggregate Concrete against Impact Loading. *Crystals* **2021**, *11*, 720. https://doi.org/10.3390/cryst11070720.
17. Yip, C.C.; Marsono, A.K.; Wong, J.Y.; Amran, M.Y.H. Flexural strength of special reinforced lightweight concrete beam for Industrialised Building System (IBS). *J. Teknol.* **2015**, *77*, 187–196. https://doi.org/10.11113/jt.v77.3505.
18. Al-Nini, A.; Nikbakht, E.; Syamsir, A.; Shafiq, N.; Mohammed, B.S.; Al-Fakih, A.; Al-Nini, W.; Amran, Y.H.M. Flexural behavior of double-skin steel tube beams filled with fiber-reinforced cementitious composite and strengthened with CFRP sheets. *Materials* **2020**, *13*, 3064. https://doi.org/10.3390/ma13143064.
19. Mohan, M.; Ramachandran, A.; Amran, M.; Borovkov, A. Determination of Buckling Behavior of Web-Stiffened Cold-Formed Steel Built-Up Column under Axial Compression. *Mater. Des.* **2022**, *15*, 2968.
20. Avudaiappan, S.; Saavedra Flores, E.I.; Araya-Letelier, G.; Thomas, W.J.; Raman, S.N.; Murali, G.; Amran, M.; Karelina, M.; Fediuk, R.; Vatin, N. Experimental investigation on composite deck slab made of cold-formed profiled steel sheeting. *Metals* **2021**, *11*, 229. https://doi.org/10.3390/met11020229.
21. Jabar, I.L.; Ismail, F. Challenges in the Management of IBS Construction Projects. *Asian J. Qual. Life* **2018**, *3*, 37. https://doi.org/10.21834/ajqol.v3i9.75.
22. Baharuddin, A.; Rahman, A.; Omar, W. Issues and Challenges in the Implemetation of Industrialised Building Systems in Malaysia. In Proceedings of the 6th Asia-Pacific Structural Engineering and Construction Conference (APSEC 2006), Kuala Lumpur, Malaysia, 5–6 September 2006.
23. Chidambaram, R.S. *Pre-Cast Concrete Connections, Issues and Innovative Solutions What is Pre-cast Structure Different Type of Connections in Pre-Cast Structure Foundation to Column Column to Column Column to Beam (Interior, Exterior, Corner) Beam to Slab*; Academy of Scientific and Innovative Research: Chennai, India, 2018.
24. Zhang, C.; Ding, K.; He, S. Seismic Performance of Panel Connectors with Steel Frame Based on Autoclaved Lightweight Concrete (ALC). *Buildings* **2022**, *12*, 372.
25. Al-sabah, S.; Laefer, D.F.; Hong, L.T.; Huynh, M.P.; Shemshadian, M.E.; Dizon, R. Introduction of the Intermeshed Steel Connection—A New Universal Steel Connection. *Buildings* **2020**, *10*, 37.
26. Cho, B.; Lee, J.; Kim, H.; Kim, D. Structural Performance of a New Blind-Bolted Frame Modular Beam-Column Connection under Lateral Loading. *Appl. Sci.* **2019**, *9*, 1929.
27. Ma, W.; Li, Y.; Ding, K.; Cheng, B.; Liu, J.; Hao, J. Mechanical Properties of New Dry-Type Beam-Column Bolt Connection Joint. *Sustainability* **2019**, *11*, 3348.
28. Lacerda, M.M.S.; da Silva, T.J.; Alva, G.M.S.; de Lima, M.C.V. Influence of the vertical grouting in the interface between corbel and beam in beam-to-column connections of precast concrete structures—An experimental analysis. *Eng. Struct.* **2018**, *172*, 201–213. https://doi.org/10.1016/j.engstruct.2018.05.113.
29. Al-Salloum, Y.A.; Alrubaidi, M.A.; Elsanadedy, H.M.; Almusallam, T.H.; Iqbal, R.A. Strengthening of precast RC beam-column connections for progressive collapse mitigation using bolted steel plates. *Eng. Struct.* **2018**, *161*, 146–160. https://doi.org/10.1016/j.engstruct.2018.02.009.

30. Mokhtar, R. *Behaviour of Precast Beam-To-Column Connections By Using Partly Hidden Corbel*; University of Malaya: Kuala Lumpur, Malaysia, 2017.
31. Wong, J.-Y.; Marsono, A.K.; Yip, C.-C. Experimental and Numerical Validation of Flexural Behaviour of Multi-Scale Prefabricated Industrialised Building System (Ibs) Sub-Frame. *J. Teknol.* **2017**, *5*, 105–116.
32. Silvester, T.B.; Cleary, P.W. Wave Structure Interaction Using Smoothed Particle Hydrodynamics. In Proceedings of the Fifth International Conference on CFD in the Process IndustriesCSIRO, Melbourne, Australia, 13–15 December 2006; pp. 1–8.
33. van de Lindt, J.W.; Gupta, R.; Garcia, R.A.; Wilson, J. Tsunami bore forces on a compliant residential building model. *Eng. Struct.* **2009**, *31*, 2534–2539. https://doi.org/10.1016/j.engstruct.2009.05.017.
34. Shibayama, T.; Nistor, I.; St-germain, P.; Townsend, R.; Nistor, I.; Asce, M.; Townsend, R.; Shibayama, T.; Asce, M. Smoothed-Particle Hydrodynamics Numerical Modeling of Structures Impacted by Tsunami Bores. *J. Waterw. Port Coast. Ocean. Eng.* **2014**, *140*, 66–81. https://doi.org/10.1061/(ASCE)WW.1943-5460.0000225.
35. Yip, C.C.; Marsono, A.K. Structural seismic performance of reinforced concrete block system for two storeys safe house. *J. Teknol.* **2016**, *2*, 83–97.
36. Farahmandpour, O.; Marsono, A.K.; Tap, M.M.; Forouzani, P. Experimental Investigation of Tsunami Waterborne Debris Impact on Structures. *Geomate J.* **2016**, *10*, 2030–2035.
37. Yip, C.C.; Marsono, A.K.; Wong, J.Y.; Lee, S. C.Seismic Performance of Scaled Ibs Block Column For Static Nonlinear Monotonic Pushover Experimental Analysis. *J. Teknol.* **2018**, *1*, 89–106.
38. Yip, C.C.; Wong, J.Y.; Lim, X.P. Flexural Strength Test of Precast Industrialised Building System Beam-Corbel Connection. *J. Teknol.* **2019**, *5*, 69–79.
39. Farahmandpour, O.; Marsono, A.K.; Forouzani, P.; Tap, M.M.; Abu Bakar, S. Experimental simulation of tsunami surge and its interaction with coastal structure. *Int. J. Prot. Struct.* **2019**, *11*, 258–280. https://doi.org/10.1177/2041419619874082.
40. Chanson, H. Physical modelling of hydraulics. *Hydraul. Open Channel Flow* **2004**, 1, 253–274. https://doi.org/10.1016/b978-075065978-9/50021-0.
41. Durst, F. *Fluid Mechanics: An Introduction to the Theory of Fluid Flows*; Springer: Berlin/Heidelberg, Germany, 2008; ISBN 9783540713425.
42. Buckingham, E. On Physically Similar Systems: Illustrations of the Use of Dimensional Equations. *Phys. Rev.* **1914**, *4*, 345–376.
43. *ASTM C150-05*; Standard Specification for Portland Cement. ASTM International: Conshohocken, PA, USA, 2005. https://doi.org/10.1520/C0150-05.
44. *BS12:1991*; Specification for Portland Cement. British Standards Institution: London, UK, 1991.
45. Auwalu, A.S.; Marsono, A.K.; Md Tahir, M.; Sulaiman, A. Behavior of cold-formed ferrocement composite column under axial loading. *J. Crit. Rev.* **2020**, *7*, 926–932. https://doi.org/10.31838/jcr.07.05.190.
46. *ASTM C33-03*; Materials, A.S. for T. and Standard and Specifications for Concrete Aggregates. Publisher: Philadelphia, PA, USA, 2003.
47. *C778-02*; Standard Specification for Standard Sand. ASTM International: Conshohocken, PA, USA, 2002.
48. *ASTM C496-96*; Standard Test Method for Splitting Tensile Strength of Cylindrical Concrete Specimens. ASTM International: Conshohocken, PA, USA, 1996.
49. *ASTMC39/C39-11a*; Standard Test Method for Compressive Strength of Cylindrical Concrete Specimens. ASTM International: Conshohocken, PA, USA,, 2011.
50. Harris, H.G.; Sabnis, G. *Structural Modling and Expeimental Techniques*, 2nd.; CRC Press: NewYork, NY, USA, 1999.
51. *ACI Committee 444 Models of Concrete Structures*; American Concrete Institute: Farmington Hills, MI, USA, 1982.
52. Negro, P.; Editors, G.T.; *Toniolo*, G. *Design Guidelines for Connections of Precast Structures under Seismic Actions*; European Commission: Brussels, Belgium, 2012; ISBN 9789279252501.
53. Weerasuriya, A.U. Computational Fluid Dynamic (CFD) simulation of flow around tall buildings. *Eng. J. Inst. Eng. Sri Lanka* **2013**, *46*, 43. https://doi.org/10.4038/engineer.v46i3.6784.
54. FEMA. *Guidelines for Design of Structures for Vertical Evacuation from Tsunamis*, 2nd ed.; (FEMA P-646); FEMA: Washington, DC, USA, 2012. https://doi.org/10.1061/40978(313)7.
55. FEMA. *Coastal Construction Manual: FEMA P-55*; FEMA: Washington, DC, USA, 2011; Volume 2, p. 400.
56. Aghl, P.P. *Determination of Demands Resulting From High Mass , Low Velocity Debris Impact on Structures*; Lehigh University Libraray: Bethlehem, PA, USA, 2014.